EU-MET-EOSMLS-PRECISION
JPL D-16160
EOS MLS DRL 601 (part 4)
ATBD-MLS-04

Earth Observing System (EOS)

Microwave Limb Sounder (MLS)

EOS MLS Retrieved Geophysical Parameter Precision Estimates

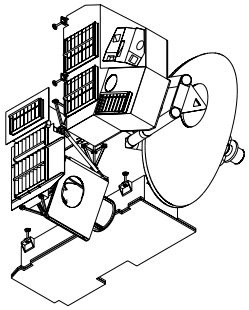

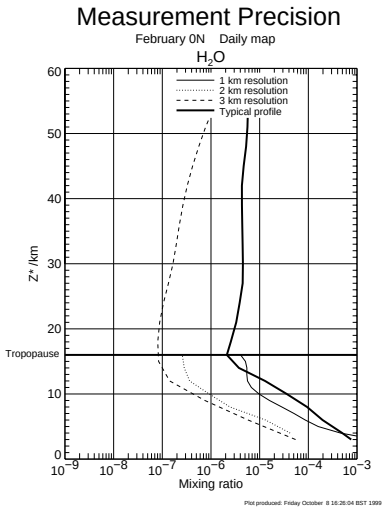

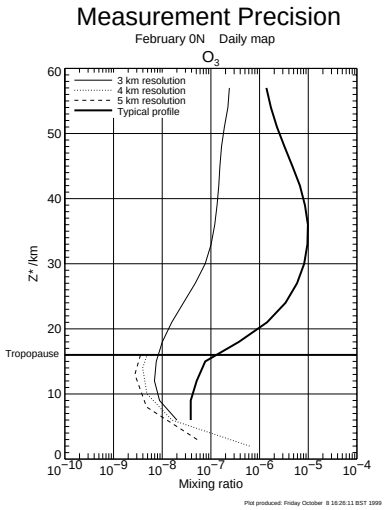

Mark J. Filipiak

Version 1.1

15 October 1999

Department of Meteorology
University of Edinburgh
King's Buildings
Edinburgh EH9 3JZ, UK

Release Record

Version	date released	comments
1.0	15 Jan 1999	Initial version
1.1	11 Oct 1999	Released following formal review of Version 1.0 by NASA board reviewing the EOS CHEM Algorithm Theoretical Basis Documents. This document received top grade of 'A' from the review board, but some changes were recommended. The board recommendations which apply to this document are italicised below, followed by the (non-italicised) responses of the MLS team. • *Vertical resolution and the approach to enhancing it should be carefully analysed and validated. Averaging kernels calculated on a high resolution grid (with finer spacing than used in the retrieval if necessary) are critical in this regard. In addition, retrieval simulations on detailed high-resolution synthetic radiance profiles with realistic noise and systematic error values should be studied, the ability to retrieve at higher resolution verified and quantified and constraint effects clearly described. This is critical to low-altitude data quality. Detailed, full, blind retrieval simulations should be done to verify expected performance. It must be demonstrated that the spectral information from well resolved lines provides the additional information necessary to achieve the desired 2 km resolution from a 4–6 km field-of-view.* Averaging kernels have been calculated on a ∼0.5 km grid and the high vertical resolution possible for H_2O and temperature in the troposphere verified and analysed (see Section 5). Blind retrieval simulations and detailed sensitivity studies are planned after the operational software is more mature; the results will be documented in later versions of this document. Changes from Version 1.0 are described below. General changes: 1. Scan program updated to conform with that shown in Waters (1999). 2. Zonal means for HO_2 corrected: these were day+night averages, but HO_2 has a strong diurnal variation. 3. Scene brightness temperature added to T_{sys} to give the total radiance noise. 4. Discussion of the resolution of H_2O and temperature in the troposphere added, including plots of averaging kernels on a 0.5 km grid. Emphasised throughout that reported resolution is *grid* resolution. Additional detailed changes, apart from minor additions/rewordings (in order of appearance in document): 1. Updated Section 2.1 introduction to make plain that profile of radiance and boresight angle is measured. 2. Added Section 2.5 explaining averaging kernels. 3. In Section3.4 the radiance uncertainty is now computed from a sum of the limb brightness temperature and the system noise temperature. 4. Added Section 3.7 and Table 2 with information on the values of *a priori* used in the averaging kernels. Updated Section 3.6 to emphasise that these *a priori* values were for the precision estimates. 5. Added Section 3.9 on the averaging kernel calculation. 6. In Section 4.1 made explicit that for varying resolution calculations, the resolution was varied only for the measurement shown. 7. Added Section 5 discussing the resolution of H_2O and temperature in the troposphere, and included plots of averaging kernels. 8. Table 3 and all plots updated with results using new formula for radiance uncertainty.

Contents

List of Tables

List of Figures

1 Scope and relation to other documents

This document reports the precision of EOS MLS in the troposphere and stratosphere, estimated from simulations of the EOS MLS measurement process. The reader is referred to Waters (1999) for an overview of the EOS MLS experiment.

The simulations use a model of the measurement process, based on the parameters given by Waters (1999). While the model makes some approximations of geophysical and instrumental effects, the results should be representative of the measurement capabilities of EOS MLS. The major limitation of the simulations is the treatment of cirrus (and other) clouds. In most of the simulations a clear atmosphere is assumed. For calculating the sensitivity to cirrus ice water content, and for calculating the effects of thick cirrus on the sensitivity to other tropospheric species, scattering in the cirrus clouds is neglected and only absorption and emission are considered, which is valid only for clouds with particle diameters less than $\sim$100 μm (Dong Wu, personal communication). Liquid water clouds have not been included. Although these absorb strongly in the frequency region used by EOS MLS, they generally occur below the targeted altitude range.

These types of simulations have helped guide some of the EOS MLS instrument design, e.g. feasibility of measuring particular chemical species and placement of spectrometer channels. The current simulations will be useful in planning the scientific exploitation of the EOS MLS data, and can serve as a 'reference' to check against the measurement capability in actual operation.

2 Introduction to the simulation model

2.1 EOS MLS

EOS MLS measures electromagnetic radiation emitted from the Earth's atmosphere in the frequency regions 100–600 GHz and 2.5 THz (Waters 1999). The radiances are measured at a series of boresight angles (equivalent to tangent heights or tangent pressures). The measured radiances as a function of boresight angle can be inverted (Livesey and Wu 1999) to derive profiles of geophysical parameters (the Data Products): chemical mixing ratios, temperature, geopotential height and ice water content (IWC). Tangent pressure, although not a Data Product, is also required as a geophysical parameter in the inversion (equivalently, tangent height could be used).

The 'measurement chain' for EOS MLS is:

- Atmosphere: chemical mixing ratios and temperature (x), as functions of pressure (p)

$\downarrow$ radiative transitions between rotational states of molecules

- local absorption, emission and scattering coefficients of radiation in the GHz and THz bands

$\downarrow$ radiative transfer in direction of EOS MLS, integration over the field-of-view (FOV) of the primary antenna, and scanning of primary antenna boresight vertically

- profile (with respect to boresight angle) of radiance (I) collected in the FOV of EOS MLS

↓ frequency down-conversion, frequency analysis in spectrometer, detection and integration during each integration period i, measurement of limb tangent height (h_i) of each integration period

- raw radiance profile (I_i), limb tangent height profile (h_i)

↓ calibration

- calibrated radiance profile (I_i), radiance uncertainty covariance matrix ($\mathbf{S_y}$), calibrated limb tangent height profile (h_i), tangent height uncertainty covariance matrix ($\mathbf{S_h}$)

↓ retrieval (inversion) process, perhaps with iterations

- estimated geophysical parameters (Data Products) (x), geophysical parameter uncertainty covariance matrix (i.e. precision) ($\mathbf{S_x}$)

For the purposes of estimating the precision of the geophysical parameters, the important parts of this process are the estimates of the radiance and tangent height uncertainty, and enough of the retrieval process to transform the radiance and tangent height uncertainty into geophysical parameter uncertainty.

2.2 Radiance uncertainty estimates

The radiance uncertainty estimates in the simulations are based on the 'Maximum Expected Noise' estimates given in Table 5-2 of Waters (1999). These estimates are used to construct the radiance uncertainty covariance matrix $\mathbf{S_y}$ required in the retrieval process (see Section 3.4).

2.3 Tangent height uncertainty estimates

The tangent height uncertainty estimates in the simulations are based on the values given for elevation angle (χ) uncertainties in Section 5.5 of Waters (1999), transforming from χ to tangent height h by scaling with the nominal tangent-point-to-EOSMLS distance for a 16 km tangent height (3062 km). The resulting tangent height uncertainty is then used to construct the tangent height uncertainty covariance matrix $\mathbf{S_h}$ required in the retrieval process (see Section 3.5).

2.4 Retrieval process

The method to be used in EOS MLS to invert the radiances and tangent heights to give geophysical parameters (Livesey and Wu 1999) is optimal estimation (Rodgers 1976). One of the products of this method is an estimate of the uncertainty in the geophysical parameters. This uncertainty is given as a covariance matrix $\mathbf{S_x}$, where usually there are correlations between errors at different levels of any one geophysical parameter (because of the limited vertical resolution of EOS MLS), and often there are correlations between errors in different geophysical parameters (e.g. because of overlapping spectral lines). The diagonal elements of $\mathbf{S_x}$ are used as the precision estimates.

The formula for $\mathbf{S_x}$ is

$$\mathbf{S_x} = (\mathbf{S_a}^{-1} + \mathbf{K}^T \mathbf{S_y}^{-1} \mathbf{K} + \mathbf{K_h}^T \mathbf{S_h}^{-1} \mathbf{K_h})^{-1}, \quad (1)$$

where $\mathbf{S_y}$ is the radiance uncertainty covariance matrix, $\mathbf{S_h}$ is the tangent height uncertainty covariance matrix, $\mathbf{K}$ is the matrix of sensitivities of radiance to changes in geophysical and instrumental parameters, $\mathbf{K_h}$ is the matrix of sensitivities of tangent height to changes in geophysical and instrumental parameters, and $\mathbf{S_a}$ is the *a priori* uncertainty covariance matrix. In this equation, the measurement process has already been discretised: the radiances (and tangent heights, of course) are measured at discrete tangent heights (integration periods) and the geophysical parameters are given as coefficients of a set of basis functions. The simulation model assumes that the atmosphere is locally spherically homogeneous, so the geophysical parameters in each profile are functions of pressure only, and uses basis functions that are triangular in log(pressure) to give piecewise linear profiles.

The sensitivity matrix $\mathbf{K}$ is the discretisation of the functional derivative

$$\frac{\delta I(b,\, j,\, \chi_i)}{\delta x_l(p_m)} \tag{2}$$

for geophysical parameters, or the partial derivative

$$\frac{\partial I(b,\, j,\, \chi_i)}{\partial p_i} \tag{3}$$

for FOV tangent pressure p_i, where $I(b,\, j,\, \chi_i)$ is the FOV-averaged and filter-averaged radiance at EOS MLS, for FOV boresight angle χ_i, filter j of band b, and $x_l(p_m)$ is the lth geophysical parameter at pressure p_m. Since the GHz and THz modules have separate scans, there are two separate sets of tangent pressure derivatives.

The sensitivity matrix $\mathbf{K_h}$ is the discretisation of the functional derivative

$$\frac{\delta h(\chi_i)}{\delta x_l(p_m)} \tag{4}$$

for geophysical parameters, or the partial derivative

$$\frac{\partial h(\chi_i)}{\partial p_i} \tag{5}$$

for FOV tangent pressure p_i, where $h(\chi_i)$ is the tangent height for FOV boresight angle χ_i and $x_l(p_m)$ is the lth geophysical parameter at pressure p_m. Since the GHz and THz modules have separate scans, there are two separate sets of tangent pressure derivatives.

In the operational retrieval, $\mathbf{S_y}$ and $\mathbf{S_h}$ are estimated in the Level 1 processing (Jarnot 1999), and the $\mathbf{K}$ and $\mathbf{K_h}$ matrices will be calculated using the model described by Read (1999). For the simulations, the values given by Waters (1999, Table 5-2 and Section 5.5) are used to construct $\mathbf{S_y}$ and $\mathbf{S_h}$, and the $\mathbf{K}$ and $\mathbf{K_h}$ matrices are calculated for a typical atmosphere and nominal instrumental characteristics.

The *a priori* uncertainty covariance matrix, as its name suggests, is the matrix of the variability of the geophysical or instrumental parameters, derived from climatology or a (large) set of previous measurements. In practice, only limited information is available and the *a priori* can better be considered a stabiliser/regulariser for the inversion of $(\mathbf{K}^T\mathbf{S_y}^{-1}\mathbf{K} + \mathbf{K_h}^T\mathbf{S_h}^{-1}\mathbf{K_h})$. For the simulations of precision, a very simple *a priori* matrix is used for the geophysical parameters, with no correlations between parameters, nor between vertical levels for each parameter (i.e. the matrix is diagonal). There is a trade-off between stabilising the inversion and biasing the retrieved parameters and uncertainties with the *a priori* values. For these simulations, the variability of the geophysical parameters is made large so that the estimated precision reflects the basic measurement capability of EOS MLS, but not so large as to destabilise the inversion.

2.5 Averaging kernels

The diagonal elements of $\mathbf{S_x}$ give the precision estimates at a specified vertical resolution (set by the basis functions used to represent the geophysical parameters). Averaging kernels (Rodgers 1990) can be used to estimate the vertical resolution at a fixed precision. The averaging kernel matrix $\mathbf{A}$ is given by

$$\mathbf{A} = \mathbf{I} - (\mathbf{S_a}^{-1} + \mathbf{K}^T\mathbf{S_y}^{-1}\mathbf{K} + \mathbf{K_h}^T\mathbf{S_h}^{-1}\mathbf{K_h})^{-1}\mathbf{S_a}^{-1}. \quad (6)$$

$\mathbf{A}$ is symmetrical and in these simulations is arranged so that the rows (and columns) are ordered by geophysical parameter then vertical level, i.e. the matrix can be partitioned into blocks corresponding to pairs of geophysical parameters. Considering one such block, each row within this is the averaging kernel for that level of the 'row' geophysical parameter with respect to the 'column' geophysical parameter. The averaging kernel quantifies how the measurement system averages the true values of geophysical parameters (i.e. columns of $\mathbf{A}$) to give the measured values (i.e. rows of $\mathbf{A}$); for an ideal measurement system, $\mathbf{A}$ would be the identity matrix. Although there may be some contribution to the measured value of the 'row' geophysical parameter at a particular level from other ('column') geophysical parameters, the useful quantity for investigating resolution is the averaging kernel for identical 'row' and 'column' geophysical parameters (i.e., on the diagonal of $\mathbf{A}$)

The fixed precision is set by (and approximately equal to) the magnitude of the elements of $\mathbf{S_a}$, which is diagonal so as not to introduce any extra smoothing. Note that $\mathbf{S_a}$ is *not* the same as in the precision estimates. For this version of the document, the averaging kernels are computed only for H_2O and temperature (averaging kernels for the other measurements will be added in a future version of the document). In each case the respective elements of $\mathbf{S_a}$ are set to the square of the chosen precision. The other elements are set to the values used for the precision estimate calculations.

To investigate vertical resolution, Equation (6) has to be calculated on a fine grid. A fine grid ($\sim$0.5 km) is used for the geophysical parameter for which the averaging kernels are required, all others are retrieved at the 'standard' resolution used for the precision estimates. The $\mathbf{K}$ matrices for the averaging kernels are calculated at $\sim$0.5 km resolution.

3 Details of the simulation model

3.1 Introduction

The major part of the simulation is the calculation of the sensitivity matrix $\mathbf{K}$. Calculating $\mathbf{K}$ requires a forward model, which is the model of the first part of the EOS MLS measurement process, from the atmosphere to calibrated radiances. The details and background to the forward model used operationally in EOS MLS are given by Read (1999) (and for UARS MLS by Read (1988) and Read and Shippony (1991)). The forward model used to create the $\mathbf{K}$ matrix for estimating precision includes the same physical effects and processes, but more approximately.

The calculation of $\mathbf{K_h}$ also requires a forward model; this is much simpler than that for $\mathbf{K}$ and is described in Section 3.3.

The power received at the detector, due to radiance received from atmospheric emission, is

$$\begin{aligned} P(b,\, j,\, \mathbf{\Omega}) \;\; = \;\; & \int_{-\infty}^{\infty} F^{+}_{b,j}(\nu) \frac{1}{4\pi} \oint_{4\pi} G^{+}_{b,j}(\mathbf{\Omega},\, \mathbf{\Omega}')\, \lambda^2 \frac{1}{2} I\,(\nu,\, \mathbf{\Omega}')\, d\Omega'\, d\nu \\ & + \int_{-\infty}^{\infty} F^{-}_{b,j}(\nu) \frac{1}{4\pi} \oint_{4\pi} G^{-}_{b,j}(\mathbf{\Omega},\, \mathbf{\Omega}')\, \lambda^2 \frac{1}{2} I\,(\nu,\, \mathbf{\Omega}')\, d\Omega'\, d\nu. \end{aligned} \tag{7}$$

$P(b,\, j,\, \mathbf{\Omega})$ is the power (W) received in filter j of band b, when the antenna boresight is pointing in direction $\mathbf{\Omega}$. $F^{\pm}_{b,j}(\nu)$ is the system spectral response for filter j of band b in the upper/lower sidebands. $G^{\pm}_{b,j}(\mathbf{\Omega},\, \mathbf{\Omega}')$ is the antenna gain function, normalised by

$$\oint_{4\pi} G^{\pm}_{b,j}(\mathbf{\Omega},\, \mathbf{\Omega}')\, d\Omega' = 4\pi. \tag{8}$$

$G^{\pm}_{i}(\mathbf{\Omega},\, \mathbf{\Omega}')$ are sufficiently weak functions of frequency that they can be calculated at the centre of the filter j of band b, but have to be separated into sidebands, since the sideband separation can be 30 GHz at 190 GHz, for example. $I\,(\nu,\, \mathbf{\Omega}')$ is the radiance ($\mathrm{W\,sr^{-1}\,m^{-2}\,Hz^{-1}}$) coming into the antenna from direction $\mathbf{\Omega}'$ at frequency ν. λ is the wavelength (m) of the radiation, and the factor of $1/2$ is required as each radiometer is sensitive to only one polarisation.

The system noise temperatures given in Table 5-2 of Waters (1999) are referred to the primary antenna and so include all the effects of losses, gains, mixer and amplifier noise. The relevant quantity to compare with this noise to get precision estimates is the brightness temperature (K), averaged (not integrated) over the normalised filter response and averaged over the FOV response. Writing brightness temperature I^* as

$$I^* = \frac{c^2}{2\nu^2 k} I, \tag{9}$$

Equation (7) leads to the following equation for the averaged I^*:

$$\begin{aligned} \overline{I^*}(b,\, j,\, \mathbf{\Omega}) \;\; = \;\; & \int_{-\infty}^{\infty} \overline{F^{+}_{b,j}}(\nu) \frac{1}{4\pi} \int_{4\pi} G^{+}_{b,j}(\mathbf{\Omega},\, \mathbf{\Omega}')\, I^*(\nu,\, \mathbf{\Omega}')\, d\Omega'\, d\nu \\ & + \int_{-\infty}^{\infty} \overline{F^{-}_{b,j}}(\nu) \frac{1}{4\pi} \int_{4\pi} G^{-}_{b,j}(\mathbf{\Omega},\, \mathbf{\Omega}')\, I^*(\nu,\, \mathbf{\Omega}')\, d\Omega'\, d\nu, \end{aligned} \tag{10}$$

where

$$\overline{F^{\pm}_{b,j}}(\nu) = \frac{F^{\pm}_{b,j}(\nu)}{\int_{-\infty}^{\infty} F^{\pm}_{b,j}(\nu)\, d\nu}. \tag{11}$$

Further, assuming that the atmosphere is spherically homogeneous in the (horizontal) direction perpendicular to the FOV boresight, the solid angle dependence can be integrated out to a vertical angle dependence (e.g. as done on UARS MLS):

$$\begin{aligned} \overline{I^*}(b,\, j,\, \chi) \;\; = \;\; & \int_{-\infty}^{\infty} \overline{F^{+}_{b,j}}(\nu) \int_{-\pi}^{\pi} \overline{G^{+}_{b,j}}(\chi,\, \chi')\, I^*(\nu,\, \chi')\, d\chi'\, d\nu \\ & + \int_{-\infty}^{\infty} \overline{F^{-}_{b,j}}(\nu) \int_{-\pi}^{\pi} \overline{G^{-}_{b,j}}(\chi,\, \chi')\, I^*(\nu,\, \chi')\, d\chi'\, d\nu, \end{aligned} \tag{12}$$

where χ is the boresight vertical angle and

$$\overline{G^{\pm}_{b,j}}(\chi,\, \chi') = \frac{1}{2\pi} G^{\pm}_{b,j}(\chi,\, \chi') \tag{13}$$

is the normalised FOV response. The treatment of the FOV and filter averages is dealt with in Section 3.2.5.

The brightness temperature at EOS MLS, $I^*(\nu, \chi')$, is found by solving the equation of radiative transfer[1],

$$\frac{dI^*(\nu, s)}{ds} = k(\nu, s)(J^*(\nu, s) - I^*(\nu, s)), \tag{14}$$

through the atmosphere along the ray at angle χ' to EOS MLS (refraction is not included in the simulations). s is the path length along the ray, $k(\nu, s)$ is the absorption coefficient and $J^*(\nu, s)$ is the source function. At the frequencies and altitudes of interest, local thermodynamic equilibrium holds, and so $J^*(\nu, s)$ is the Planck function in temperature units,

$$J^*(\nu, s) \equiv B^*(\nu, s) = \frac{h\nu/k}{e^{h\nu/kT(s)} - 1}. \tag{15}$$

So far the brightness temperature, $\overline{I^*}(b, j, \chi)$, at the primary antenna has been discussed. For the precision estimates, the derivative of $\overline{I^*}(b, j, \chi)$ with respect to geophysical and instrumental parameters is required, and this is calculated by perturbation, as described below in Section 3.2.6.

3.2 Parts of the forward model (sensitivity model) for radiance

3.2.1 Geometry

The angle χ can be transformed to tangent height z given the satellite orbital radius (7083 km), Earth radius (6371 km), and assuming spherical symmetry and no refraction. In the simulation model, the transformation from χ to tangent height z is approximated by scaling with the nominal tangent-point-to-EOSMLS distance for a 16 km tangent height (3062 km).

With this transformation, the brightness temperature I^* is now a function of tangent height z:

$$\begin{aligned}\overline{I^*}(b, j, z) \;=\; & \int_{-\infty}^{\infty} \overline{F^+_{b,j}}(\nu) \int_{-\infty}^{\infty} \overline{G^+_{b,j}}(z, z')\, I^*(\nu, z')\, dz'\, d\nu \\ & + \int_{-\infty}^{\infty} \overline{F^-_{b,j}}(\nu) \int_{-\infty}^{\infty} \overline{G^-_{b,j}}(z, z')\, I^*(\nu, z')\, dz'\, d\nu,\end{aligned} \tag{16}$$

and the integration of the radiative transfer equation for $I^*(\nu, z')$ is now along the ray tangent at height z'.

3.2.2 Atmosphere

To calculate I^* and $\delta I^*/\delta x(p)$, a model atmosphere is required. The simulation model assumes that the atmosphere is locally spherically homogeneous, so the atmospheric parameters are functions of pressure only. Most of the atmospheric parameters (temperature and chemical mixing ratios as a function of pressure) come from a run of the THINAIR model for the year 2003 (see Kinnersley and Harwood (1993) for a description of an earlier version of this model). The THINAIR model produces daylight averaged values, in

[1] The precision model does not yet include scattering from ice clouds.

the vertical range $z^* = 0$ km* to $z^* = 100$ km*. ($z^* = H \log_{10}(p_0/p)$ with p = pressure, $p_0 = 1000$ hPa and $H = 16$ km. To differentiate pressure height and geometric height, the unit for pressure height is written km*.) Above 60 km* the parameters are taken from Shimazaki (1985), AFGL (1985) and Hedin (1990). Some atmospheric parameters have been taken from other sources and combined with the THINAIR model climatology:

- Geopotential as a function of pressure is calculated using the hydrostatic equation, with reference geopotential set to 160000 $m^2\,s^{-2}$ at 100 hPa.

- Temperature comes from the UARS climatology (UARS Climatology 1994), and in the lower troposphere from the monthly mean values in Oort (1983).

- H_2O comes mainly from the SAGE-2/HALOE climatology (Pumphrey *et al.* 1998), with lower tropospheric values from Oort (1983). The values near the tropopause have been calculated directly from SAGE-2 profiles relative to each profile's tropopause. The resulting mean H_2O is then shifted vertically so that the SAGE-2 mean tropopause coincides with the model tropopause. For the February 0N atmosphere, the SAGE-2 profiles from 10S to 10N were averaged, and for the February 70N atmosphere, the SAGE-2 profiles from 50N to 60N were averaged. For use *only* in calculating the relative humidity uncertainty from the H_2O and temperature uncertainties, relative humidity in the troposphere was set to a constant value based on the average values in the upper troposphere from the SAGE-2 data. The values were 30% for the February 70N atmosphere and 15% for the February 0N atmosphere.

- O_3 in the troposphere was adjusted to match Muller and Brasseur (1995).

- CO was adjusted to match Muller and Brasseur (1995) in the troposphere and Solomon *et al.* (1985) in the stratosphere and mesosphere.

- ClO was adjusted to match values from UARS MLS.

- SO_2 (assuming no volcanic enhancement) is from Brasseur and Solomon (1986).

- The 'standard' atmospheres have no clouds (the sensitivity to changes in cirrus ice water content can still be calculated in this case). To test the effect of cirrus clouds on the precision of other tropospheric species (H_2O, O_3 and CO), two synthetic atmospheres with moderate and thick cirrus were used. The cirrus 'clouds' have a triangular shape in pressure height, with mean thickness 2 km*. The cloud centre is at 6 km* for the February 70N atmosphere, 14 km* for the February 0N atmosphere. For the 'moderate' cirrus case the mean IWC was 0.05 $g\,m^{-3}$; for the 'thick' cirrus case the mean IWC was 0.5 $g\,m^{-3}$. Associated with the cloud, the H_2O mixing ratio was increased to give 100% relative humidity at the cloud centre, dropping linearly to the clear-sky values at the top and bottom of the cloud.

Two 'typical' atmospheres have been chosen for the precision simulations. One is for February at the Equator with tropopause at 16 km*. This gives a tropical atmosphere near the Equinox. The other is for February at 70N with tropopause at 8 km*, with unperturbed O_3. This gives a polar winter atmosphere, but with some sunlight for chemical activation.

3.2.3 Other geophysical parameters

Gravity is taken from the Smithsonian Meteorological Tables (List 1968).

Magnetic field is disregarded in the simulations—no Zeeman splitting and consequent polarised radiative transfer is considered. Zeeman splitting is not important until the total splitting is comparable to the width of the spectral line (Doppler broadening sets the lower limit on the linewidth), and then only near the line centre. Out of the spectral lines measured by EOS MLS, Zeeman splitting by the Earth's magnetic field is large compared with the Doppler linewidth only for the 118 GHz line of O_2 (shift for the maximum $|M|$ components is $\pm$ ~1 MHz, compared with a Doppler width at 200 K of ~0.1 MHz) and the 233 GHz line of ^{18}OO (shift for the maximum $|M|$ components is $\pm$ ~3 MHz, compared with a Doppler width at 200 K of ~0.2 MHz). The OH lines in the THz region have significant Zeeman splitting (shift for the maximum $|M|$ components is $\pm$ ~1 MHz), but the Doppler width is also large (~3 MHz) at these frequencies, and the effect is a slight increase in line broadening (~2% change). The ClO lines at 204 GHz have Zeeman splitting comparable to the Doppler width, but since most of the sensitivity to ClO comes from the lines at 649 GHz, the effect on the ClO precision of ignoring the splitting in the 204 GHz lines is negligible. The possible effect of neglecting the Zeeman splitting of the O_2 and ^{18}OO lines has been (very) crudely estimated by repeating the simulations without the centre filters of the 'a' type spectrometers that are centred on these lines, and also deleting the 'c' type spectrometer that is centred on the O_2 line. The result is that the chemical species precisions are unaffected, and the geopotential height and temperature precision is slightly degraded above ~40 km*: the geopotential height uncertainty at 50 km* changes from 35 m to 37 m, and the temperature uncertainty at 50 km* changes from 3 K to 3.3 K.

3.2.4 Absorption coefficient

The spectroscopic parameters come from the JPL Catalogue (Pickett *et al.* 1992) for line frequency, linestrength and lower state energy, and from the HITRAN catalogue (Rothman *et al.* 1992) for line broadening parameters. Vibrational partition functions are included for certain species. Some (O_3, ClO, H_2O) are included in the JPL Catalogue, others (HNO_3, HCN, N_2O) have been approximated based on the lowest-lying vibrational states. The parameters for the O_2 lines at 63 GHz and 118 GHz are taken from the MPM93 model (Liebe *et al.* 1993), but where negative absorption occurs the absorption is set to zero. For frequencies less than 1000 GHz, the MPM93 H_2O line parameters are used, to be consistent with the H_2O continuum used.

Local thermodynamic equilibrium is assumed everywhere.

Line shape is van Vleck–Weisskopf (VVW), approximately convolved with Doppler (Read 1992). The approximation is to convolve only the Lorentz part of the VVW shape with the Doppler shape so that a Voigt function (Drayson code) can be used.

The H_2O continuum below 1000 GHz is taken from the MPM93 model. At 2.5 THz no separate H_2O continuum is added as the wings of strong H_2O lines in the THz frequency region dominate the 'continuum' absorption.

The empirical dry air continuum from UARS MLS (Bill Read, personal communication)

$$k_{\mathrm{dryair}} = 1.59 \times 10^{-19} p^2 (300/T)^{3.71} \nu^2 e^{-1.85\times10^{-12}\nu^2} \mathrm{km}^{-1}, \quad (17)$$

where p is pressure in hPa, T is temperature in Kelvin, and ν is frequency in MHz, is used below 1000 GHz. This includes the N_2 collision induced absorption. At 2.5 THz the dry air continuum used is the N_2 collision induced absorption from Borysow and Frommhold (1986).

Cirrus clouds are treated as another species, neglecting scattering and with absorption dependent on the ice water content (Wu, Waters and Read, document in preparation). This will be valid only for clouds having no particles with diameters $>\sim 100\mu$m. The absorption coefficient is based on the long-wave approximation of Gunn and East (1954) and the refractive index data of Hufford (1991).

3.2.5 Instrument response

$\overline{G^{\pm}_{b,j}}(z, z')$ is modelled as a Gaussian in $z - z'$, with half-power points for each radiometer LO frequency taken from Table 5-4 of Waters (1999). The frequency of the centre of the relevant sideband is then used for further scaling.

$\overline{F^{\pm}_{b,j}}(\nu)$ is modelled as a constant ($= 1/B$) in the nominal bandwidth B of filter j of band b, zero outside.

The response in the signal and image sidebands can be different, and the system noise temperature is specified for the signal sideband. For the GHz radiometers the sideband ratio is assumed to be 1 : 1 (LSB:USB) in this simulation. For the 2.5 THz radiometer the sideband ratio is not necessarily 1 : 1 because of the Fabry-Perot diplexer, and values from the Preliminary Design Review (PDR 1998) are used (these are 1 : 0.4 for the 8.4 GHz IF, 1 : 0.8 for 12.8 GHz IF, and 1 : 2 for 20.4 GHz IF).

3.2.6 Discretisation and calculation of derivatives

The atmosphere is discretised in 1 km* steps from 0 km* to 60 km*, and 10 km* steps from 60 km* to 100 km*. The absorption coefficients are calculated with the same discretisation in pressure height and interpolated linearly in pressure height between levels. Ray radiances $I^*(\nu, z')$ are calculated on a tangent height grid of 1 km*/10 km* also.

The integration of the radiative transfer equation uses an implicit 4th-order Runge-Kutta method.

Frequency was discretised on a varying resolution grid, with finest resolution at the centre of each spectrometer. For the ‘a’-type spectrometers, the grid is 30 points for the centre filter (6 MHz wide) and 5 points per filter for the other filters (8 to 96 MHz wide). The ‘b’-type spectrometers have the same grid as the ‘a’-type. Each ‘c’-type spectrometer has a grid of 1 point per filter. Each ‘d’-type spectrometer has a grid of 5 points for the one filter in the spectrometer.

The filter average is calculated using trapezoidal rule integration over the filter nominal bandwidth. The FOV average is calculated using direct convolution of the Gaussian FOV response with the ray radiance, using linear interpolation of the ray radiance between tangent heights.

Temperature, reference geopotential and chemical species mixing ratio derivatives are calculated by perturbation, keeping the tangent pressure constant. The perturbation is at one atmospheric level in turn, equivalent

to perturbation of a triangular basis function, base 2 km*, centred on the level. Temperature perturbations maintained hydrostatic balance. Pointing derivatives were calculated by perturbing the tangent height, and converting to the equivalent pressure perturbation.

With the discretisations used, the matrix of derivatives (**K** matrix) has the form

$$K = \frac{\partial I(b, j, i)}{\partial x_l(m)} \tag{18}$$

(geophysical parameters) or

$$K = \frac{\partial I(b, j, i)}{\partial p_i} \tag{19}$$

(tangent pressure), for filter j of band b, tangent level (i.e. integration period) i, parameter l and perturbation level m.

3.3 The forward model for tangent height

The forward model for tangent height is much simpler than that for radiance. The tangent heights are calculated as a by-product of the radiance forward model. The geophysical/instrumental parameters that can affect the tangent height are the reference geopotential, temperature, H_2O and tangent pressure. Although H_2O will affect the tangent height through the refractive index and, to a lesser extent, the mean molar mass, its effects are neglected in the simulations since refraction has not been included in the forward model. The effects of the other parameters can be calculated by integrating the hydrostatic equation with/without perturbed parameters.

With the discretisations used, the matrix of derivatives ($\mathbf{K_h}$ matrix) has the form

$$K_h = \frac{\partial h(i)}{\partial x_l(m)} \tag{20}$$

(geophysical parameters) or

$$K_h = \frac{\partial h(i)}{\partial p_i} \tag{21}$$

(tangent pressure), for tangent level i, parameter l and perturbation level m.

3.4 Radiance uncertainty $\mathbf{S_y}$

The radiance uncertainty is modelled using the T_{sys} values given in Waters (1999), Table 5-2.

The (single sideband) spectrally-varying component of radiance uncertainty used is given by the greater of $(T_{\text{sys}} + T_{\text{limb}}^{\text{LSB}} + T_{\text{limb}}^{\text{USB}})/\sqrt{B\tau}$ and $\Delta I_{\text{min}}/3$, where $T_{\text{limb}}^{\text{LSB}}$ is the limb brightness temperature seen through the EOS MLS antenna, for the lower sideband, $T_{\text{limb}}^{\text{USB}}$ is the limb brightness temperature for the upper sideband, B is the nominal filter bandwidth, τ is the integration time of the measurement and ΔI_{min} is a lower limit given in Waters (1999), Table 5-2 (this lower limit means that some monthly zonal mean uncertainties are not simply $1/\sqrt{30}$ times the daily zonal mean uncertainties). The spectrally-varying component of radiance

uncertainty is assumed uncorrelated between filters / DACS channels and between tangent heights (boresight angles), so its covariance matrix is completely diagonal.

The spectrally-averaged component of radiance uncertainty uses the formula given in Waters (1999), Table 5-2, Note 7. It is assumed completely correlated within a radiometer but uncorrelated between tangent heights and between radiometers, which leads to a block diagonal matrix for this component.

$\mathbf{S_y}$ has dimension = [(no. of tangents) $\times$ (no. of channels)] $\times$ [(no. of tangents) $\times$ (no. of channels)] and is the sum of the covariance due to the spectrally-varying and spectrally-averaged components of radiance uncertainty.

The treatment of integration time in the precision simulations is rather different from (but equivalent to) the operational method. Rather than using the scan program to interpolate the FOV averaged radiances/derivatives to varying tangent heights at constant integration time step (0.16 s for the nominal scan), the code keeps the tangent heights fixed at 1 km* steps and varies the integration time per km* using the scan program. Tangents above and below the scan limits are switched off by reducing their integration time to (nearly) zero. The scan programs used for the GHz and THz antennae are based on those shown in Figure 6-2 of Waters (1999). The effect of scan motion during the integration is included by locally averaging the **K** matrix.

3.5 Tangent height uncertainty $\mathbf{S_h}$

The tangent height uncertainties are based on the values given for elevation angle (χ) uncertainties in Section 5.5 of Waters (1999). The transformation from χ to tangent height h is approximated by scaling with the nominal tangent-point-to-EOSMLS distance for a 16 km tangent height (3062 km), so that a 1 arcsecond elevation uncertainty is modelled as a 15 metre tangent height uncertainty. The resulting tangent height uncertainty is divided by 3 to convert from 3σ to 1σ errors. This leads to the following values for 1σ tangent height uncertainties: absolute tangent height uncertainty = 10 m, tangent height rate uncertainty = 5 m s^{-1}, tangent height jitter = 10 m.

These values are then used to construct the tangent height uncertainty covariance matrix $\mathbf{S_h}$. $\mathbf{S_h}$ has dimension = [no. of tangents] $\times$ [no. of tangents] and is the sum of the covariance matrices due to the absolute tangent height uncertainty, tangent height rate uncertainty (converted to a tangent height uncertainty), and tangent height jitter.

For the absolute tangent height uncertainty and tangent height jitter, no correlation between the errors for different integration periods is assumed, leading to diagonal covariance matrices for these components. For the tangent height rate uncertainty, no correlation between the *rate* errors for different integration periods is assumed, leading to a non-diagonal tangent *height* covariance matrix for this component, with entries $S_{i_1 i_2} \propto \min(t_{i_1}, t_{i_2})$, where t_{i_n} is the time from the start of the scan to the start of integration period i_n.

Since the GHz and THz modules have separate scans, there are two separate covariance matrices for the tangent heights, combined as a direct sum to give a block diagonal $\mathbf{S_h}$.

The treatment of integration time for tangent height is the same as that for radiance (Section 3.4).

3.6 *A priori* uncertainty $\mathbf{S_a}$ for the precision estimates

For the precision estimates, the *a priori* uncertainty in the geophysical and instrumental parameters used is large (and constant) so that the precision estimates reflect the basic measurement capabilities of EOS MLS. The *a priori* uncertainty is kept the same for varying retrieval grid resolution and varying space/time averages.

The *a priori* uncertainties are given in Table 1. The *a priori* uncertainty is assumed uncorrelated, so $\mathbf{S_a}$ is diagonal.

Table 1: *A priori* uncertainties for precision estimates.

BrO	1000×10^{-12}
ClO	4×10^{-9}
CO	3×10^{-6}
reference geopotential	$10^5\ \mathrm{m^2\,s^{-2}}$
H_2O	10×10^{-3}
HCl	30×10^{-9}
HCN	$10\times$ model atmosphere profile
HNO_3	100×10^{-9}
HO_2	3×10^{-9}
HOCl	3×10^{-9}
IWC	$0.5\ \mathrm{g\,m^{-3}}$
N_2O	3×10^{-6}
O_3	30×10^{-6}
OH	3×10^{-9}
SO_2	1×10^{-6}
temperature	300 K

3.7 *A priori* uncertainty $\mathbf{S_a}$ for the averaging kernels

The averaging kernels are calculated for H_2O and temperature only, and for Daily Map and Daily Zonal Mean only. For these the *a priori* uncertainty is given in Table 2. The magnitude of the *a priori* uncertainty

Table 2: *A priori* uncertainties for averaging kernels.

H_2O	Daily Map	10% model atmosphere profile
H_2O	Daily Zonal Mean	10% model atmosphere profile
temperature	Daily Map	1 K
temperature	Daily Zonal Mean	1 K

sets the precision for which the averaging kernels are calculated. Based on the precision estimates (see Figures 8, 9, 25, and 26), the expected resolution in the troposphere is between 1 and 2 km for the values in Table 2. All the other geophysical parameters have the *a priori* uncertainties given in Table 1.

3.8 Precision estimate calculation

Having calculated $\mathbf{K}$, $\mathbf{K_h}$, $\mathbf{S_y}$, $\mathbf{S_h}$ and $\mathbf{S_a}$, these need to be combined in the formula for $\mathbf{S_x}$ (Equation (1)). The estimated precision is the square root of the diagonal elements of the covariance matrix $\mathbf{S_x}$.

In Equation (1) the $\mathbf{K}$ matrices for each sideband are added, with correct weighting (from the sideband ratio). Since the system noise is single-sideband, the resulting $\mathbf{K}$ matrix is used as it is, without dividing by 2.

There are several frequency regions where there are overlapping filters (see Figure 5-3 of Waters (1999)). These overlaps have been treated by deleting one of the sets of overlapping filters, usually the wider filters, from the simulation (this can result in some very small gaps or some even smaller overlaps remaining). Specifically, the centre filters of each 'c' spectrometer are used instead of the centre filter of the overlapping 'a' spectrometer. The uncertainties for space/time averages (e.g. zonal means) are calculated by averaging the radiance and tangent height uncertainties first, and using the averaged $\mathbf{S_y} + \mathbf{S_h}$ in Equation (1).

The resolution of the retrieval is varied by changing the spacing of the grid used for the retrieved geophysical parameters, rather than the alternative method of introducing correlations in the *a priori* uncertainty.

The basic resolution is 1 km*, set by the grid used in the forward model to calculate the $\mathbf{K}$ matrices. Retrievals on coarser resolution grids are made by taking weighted sums of the $\mathbf{K}$ matrix elements to produce a new $\mathbf{K}$ matrix with a reduced number of columns (perturbation levels) but the same number of tangents. For example, for 3 km* resolution, the new $\mathbf{K}$ matrix would have 20 columns for each species rather than 60, and each column (perturbation level) would correspond to a triangular basis function with base 6 km*.

The stratospheric O_3 column precision is derived from the O_3 profile precision, and, similarly, the relative humidity profile precision is derived from the H_2O and temperature precision, and the geopotential height profile precision is derived from the reference geopotential precision and the temperature precision (the effects of H_2O variations being neglected).

The stratospheric O_3 column is a weighted sum of the O_3 profile, the weights being the integrated air number density (converted to Dobson units (DU)) of each triangular basis function in the stratosphere, with corrections at the tropopause and stratopause for part-triangles, and zero outside the stratosphere. If the weights are represented by a matrix $\mathbf{L}$, and the O_3 profile covariance matrix by $\mathbf{S_{O_3}}$, then the stratospheric O_3 column uncertainty $\mathbf{S}_{\mathrm{O_3column}}$ is given by,

$$\mathbf{S}_{\mathrm{O_3column}} = \mathbf{L}^T \mathbf{S_{O_3}} \mathbf{L} \tag{22}$$

In these simulations, the tropopause is fixed at 8 km* for February 70N and 16 km* for February 0N and the stratopause is fixed at 48 km* (= 1hPa). So the 'stratospheric' O_3 column is really the O_3 column between specified *pressures*. Operationally, the tropopause pressure will be retrieved by some method yet to be determined, and the uncertainty in this tropopause pressure (and, to a lesser extent, the uncertainty in the stratopause pressure) will result in the precision of the O_3 column being worse than that reported below in Table 3. To set the scale for the contribution of the tropopause/stratopause pressure (or height) uncertainties, at the tropopause the O_3 concentration is $\sim$4 DU/km, and at the stratopause the O_3 concentration is $\sim$0.4 DU/km,

The relative humidity (RH) profile precision is treated similarly. At H_2O profile level m, RH is a function g

of the H_2O mixing ratio, pressure and temperature, and the RH covariance matrix $\mathbf{S}_{\mathrm{RH}_m}$ is given by

$$\mathbf{S}_{\mathrm{RH}_m} = \mathbf{L}_m^T \mathbf{S}_{\mathrm{H_2O}_m,\mathrm{T}_m} \mathbf{L}_m, \tag{23}$$

where $\mathbf{L}_m$ is the matrix of $\partial g/\partial \mathrm{H_2O}_m$ and $\partial g/\partial \mathrm{T}_m$ at level m, and $\mathbf{S}_{\mathrm{H_2O}_m,\mathrm{T}_m}$ is the covariance matrix for H_2O and temperature at level m only. The function g relating RH to the H_2O mixing ratio, pressure and temperature is the Goff-Gratch function for relative humidity over ice (Tables 94–97 of List (1968)).

The geopotential at pressure p is the sum of the reference geopotential (Φ_r) and a weighted sum of the temperature profile, the weights being the contribution of each triangular basis function (of the temperature profile) to the integral of the hydrostatic equation between the reference pressure and p. The geopotential height is defined as $(1/9.8)\times$geopotential. The geopotential height is calculated on a 1 km* grid, and if the weights are represented by a matrix $\mathbf{L}$ with weight $= 1$ for the reference geopotential, and the combined T and reference geopotential covariance matrix by $\mathbf{S}_{\mathbf{T},\Phi_r}$, then the geopotential height covariance matrix $\mathbf{S}_{\mathrm{GPH}}$ is given by,

$$\mathbf{S}_{\mathrm{GPH}} = \frac{1}{9.8} \mathbf{L}^T \mathbf{S}_{\mathbf{T},\Phi_r} \mathbf{L} \tag{24}$$

3.9 Averaging kernel calculation

The averaging kernel matrix $\mathbf{A}$ is calculated using Equation (6). $\mathbf{K}$, $\mathbf{K_h}$, $\mathbf{S_y}$ and $\mathbf{S_h}$ are calculated as described in the preceding sections, but on a 0.5 km* grid rather than the 1 km* grid used for the precision estimates. The resolution of the relevant geophysical parameter (H_2O or temperature) is kept at the basic resolution of the grid (0.5 km*), and $\mathbf{S_a}$ is constructed from the values in Tables 1 and 2. The treatment of sidebands, overlapping filters and space/time averages is exactly the same as for the precision estimate calculations.

To estimate vertical resolution, it is sufficient to look at the diagonal blocks of $\mathbf{A}$ corresponding to each geophysical parameter, i.e., ignoring any cross-correlations between geophysical parameters. The averaging kernels shown in Figures 27–28 are the rows of the relevant diagonal block.

4 Precision estimates

4.1 General Description

In Figures 1 to 26, plots of estimated precision *vs.* height are given for the vertical profiles of the geophysical parameters measured by EOS MLS. Table 3 gives the estimated precision of the stratospheric O_3 column measurements, neglecting the contribution due to the uncertainty in knowledge of the tropopause and stratopause pressures.

For each geophysical parameter there is a figure containing plots using the ‘standard’ atmospheres and vertical resolutions. There are two plots and some notes per figure. One plot is for the February 70N atmosphere and the other is for the February Equator atmosphere, both described in Section 3.2.2 above. The resolution is the spacing of the retrieval grid used, *not* the inverse of the highest spatial frequency that can be represented. The vertical resolution is 3 km*, except for BrO and HCN, both at 5 km* resolution.

Apart from the OH plots, all the precision estimates are based on the timesharing mode (Waters (1999), Section 5.8) with the 240 GHz radiometer and all DACS switched on and the 2.5 THz radiometer switched off. For the OH plots, the timesharing mode is with the 240 GHz radiometer and all DACS switched off and the 2.5 THz radiometer switched on.

For some measurements, extra plots at varying vertical resolutions (in the troposphere) are given, to show the tradeoff between resolution and precision. For these the resolution was varied for only the measurement shown. In the case of H_2O and temperature, the resolution can be increased while retaining acceptable precision. In the case of CO and O_3, the resolution can be decreased to achieve better precision.

The effect of thick cirrus clouds on the precision of the tropospheric measurements of CO, H_2O and O_3 is shown in Figures 5, 10 and 21. The effect is probably underestimated, since scattering has not been included in the simulations.

On each plot the vertical axis is pressure height in km* ($= 16 \log_{10}(1000/p)$ with p in hPa). The vertical range of the plots is from 0 km* to 60 km* to correspond to the nominal scan pattern. The horizontal axis is the estimated precision, which is the square root of the diagonal elements of the covariance matrix $\mathbf{S_x}$.

The precision estimates are for various space/time averages:

single profile no averaging, derived from one radiance profile,

daily map 3 profile average, $\sim 5^\circ$ latitude resolution,

daily zonal mean 5° zone, diurnally-varying species split into day and night, non-diurnally-varying species averaged over day and night,

monthly map approximately 5° latitude, 20° longitude resolution at mid-latitudes for diurnally-varying species, 5° latitude, 10° longitude resolution at mid-latitudes for non-diurnally-varying species,

monthly zonal mean 5° zone, diurnally-varying species split into day and night, non-diurnally-varying species averaged over day and night.

A typical profile (the one in the model atmosphere) is also plotted to set the scale.

4.2 Stratospheric O_3 Column

Table 3: Stratospheric O_3 column precision, for varying space/time averages, with typical values and sensitivity to changes in tropopause and stratopause heights. The precision values do not include any contribution from uncertainties in the tropopause and stratopause heights: the tropopause is fixed at 8 km* for February 70N and 16 km* for February 0N; the stratopause is fixed at 48 km*.

	Stratospheric O_3 Column							
	precision /DU					typical value /DU	tropopause height sensitivity /(DU/km)	stratopause height sensitivity /(DU/km)
	single profile	daily map	daily zonal mean	monthly map	monthly zonal mean			
February 70N	1.9	1.2	0.20	0.23	0.096	311	4	0.4
February 0N	0.91	0.56	0.096	0.11	0.027	212	4	0.4

4.3 Plots of estimated precision

Plots of the precision estimates are given on the following pages. The plots are in alphabetical order of the parameter name (with the exception of Relative Humidity, which is just after the H_2O plots).

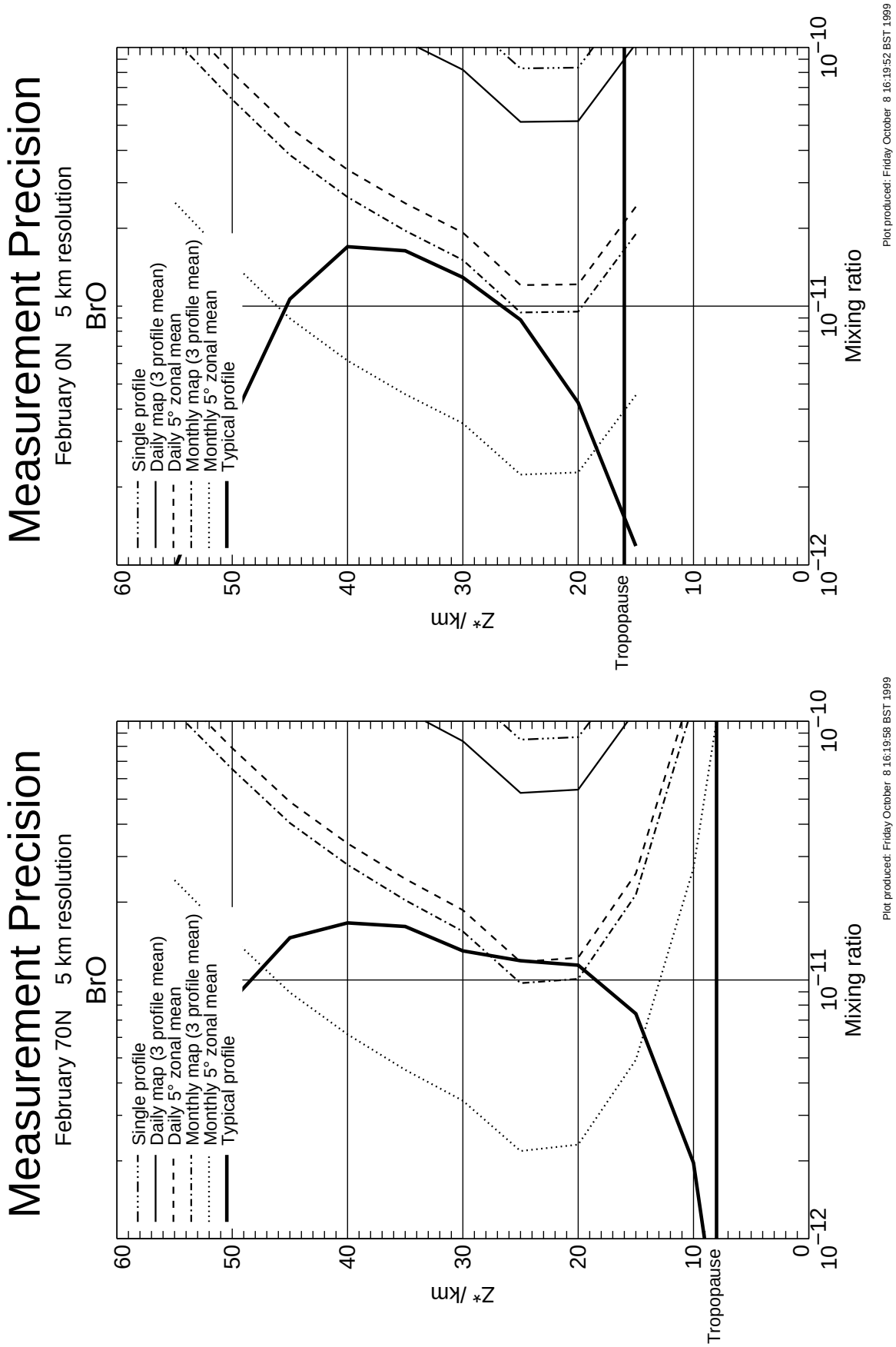

Figure 1: BrO precision at 5 km vertical resolution, for varying space/time averages.

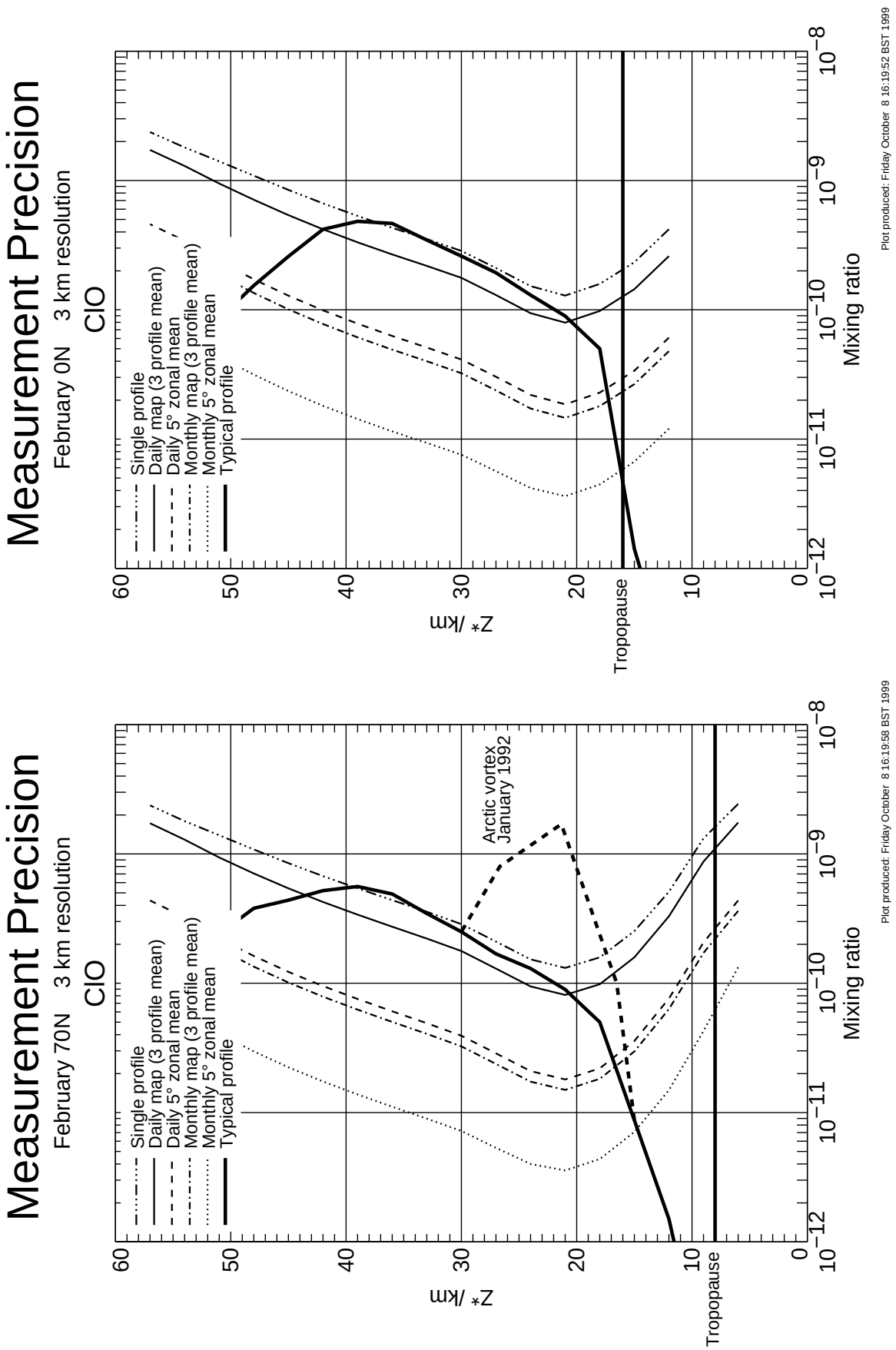

Figure 2: ClO precision at 3 km vertical resolution, for varying space/time averages. The enhanced ClO profile comes from UARS MLS measurements for January 1992, averaged over the Arctic vortex (Waters *et al.* 1996).

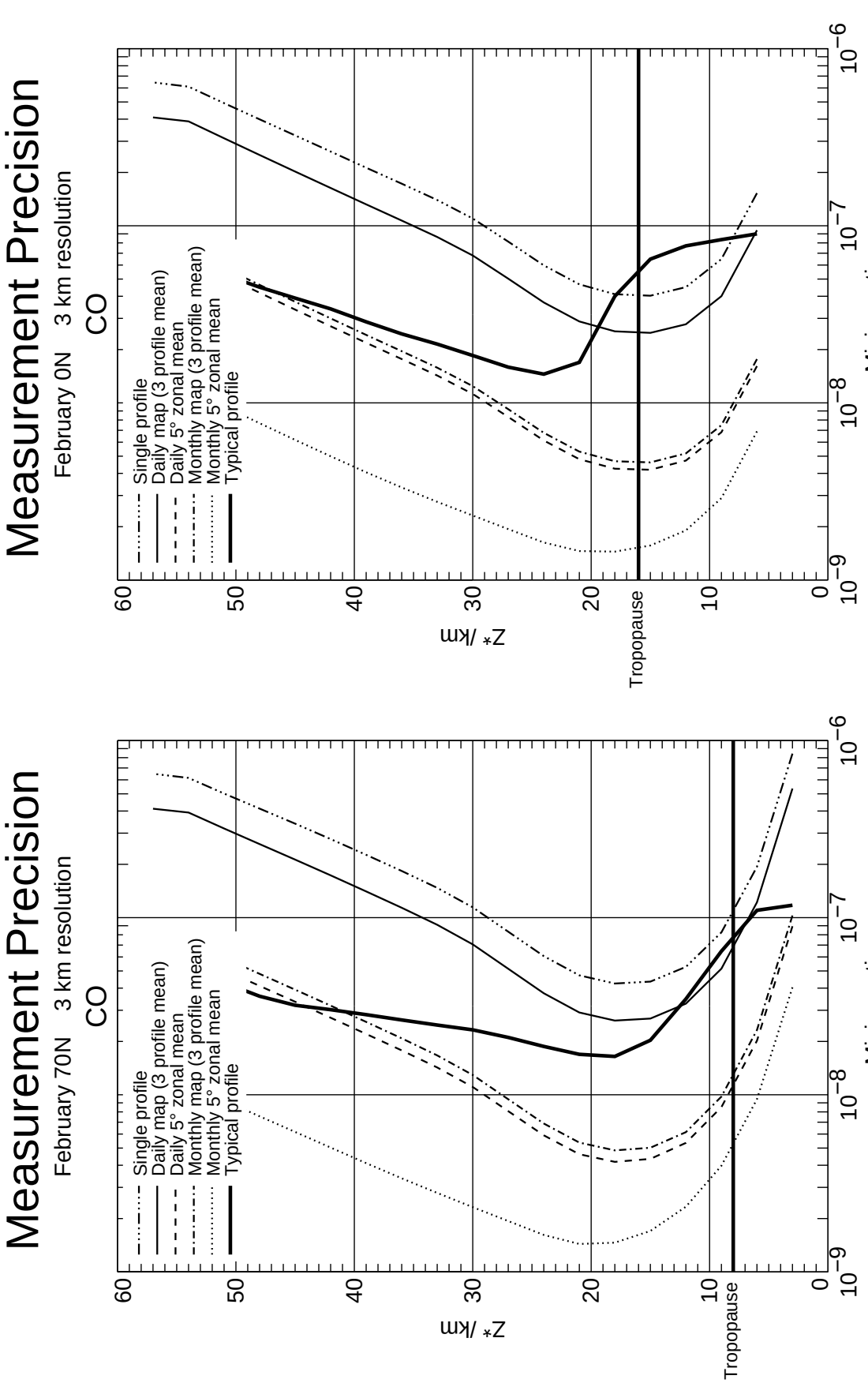

Figure 3: CO precision at 3 km vertical resolution, for varying space/time averages. (Note: the CO mixing ratio increases rapidly above 60 km, to more than 10^{-5} above ~80 km (e.g., Waters *et al.* 1976), and EOS MLS is expected to provide useful CO measurements up to ~100 km.)

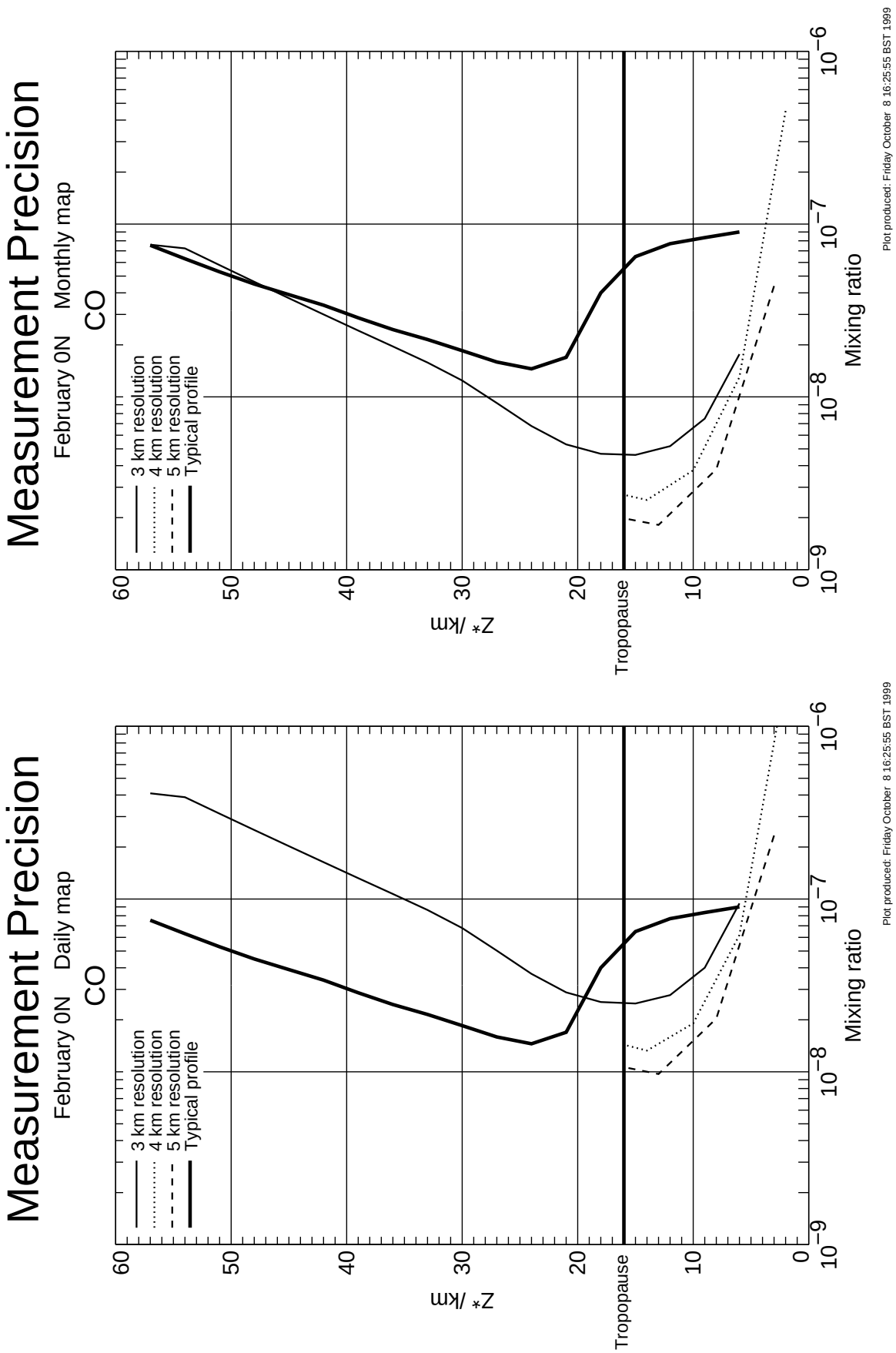

Figure 4: CO precision at 3, 4, 5 km vertical resolution in the troposphere, for Daily Map and Monthly Map (February Equator only). The resolution in the stratosphere remains 3 km.

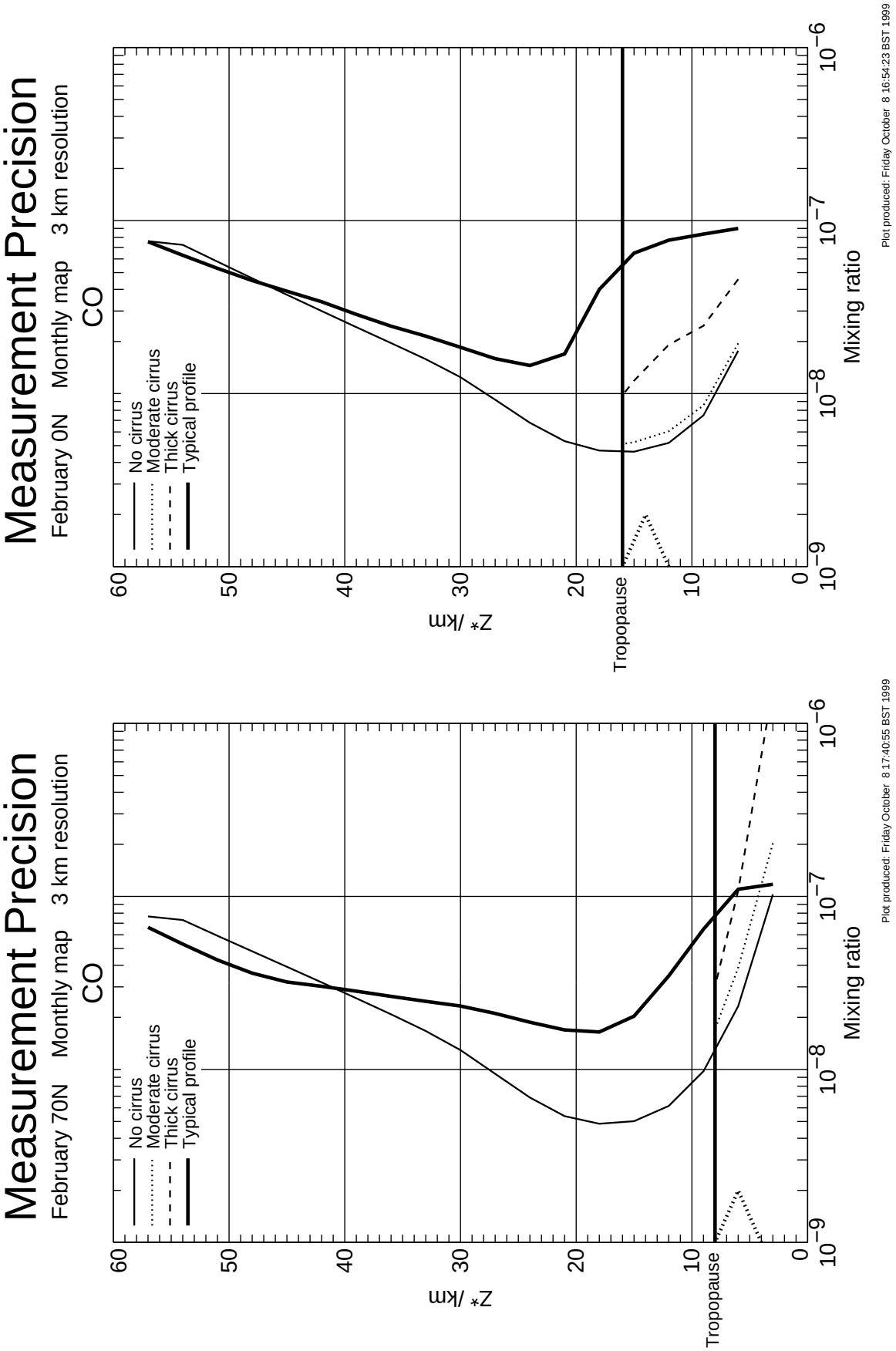

Figure 5: The effect of cirrus clouds (without scattering) on CO precision in the troposphere, for Monthly Map only. The vertical resolution is 3 km. On the left of each plot is an indication of the position and shape of the cirrus cloud. Moderate cirrus has IWC=0.05 g m^{-3}, thick cirrus has IWC=0.5 g m^{-3}.

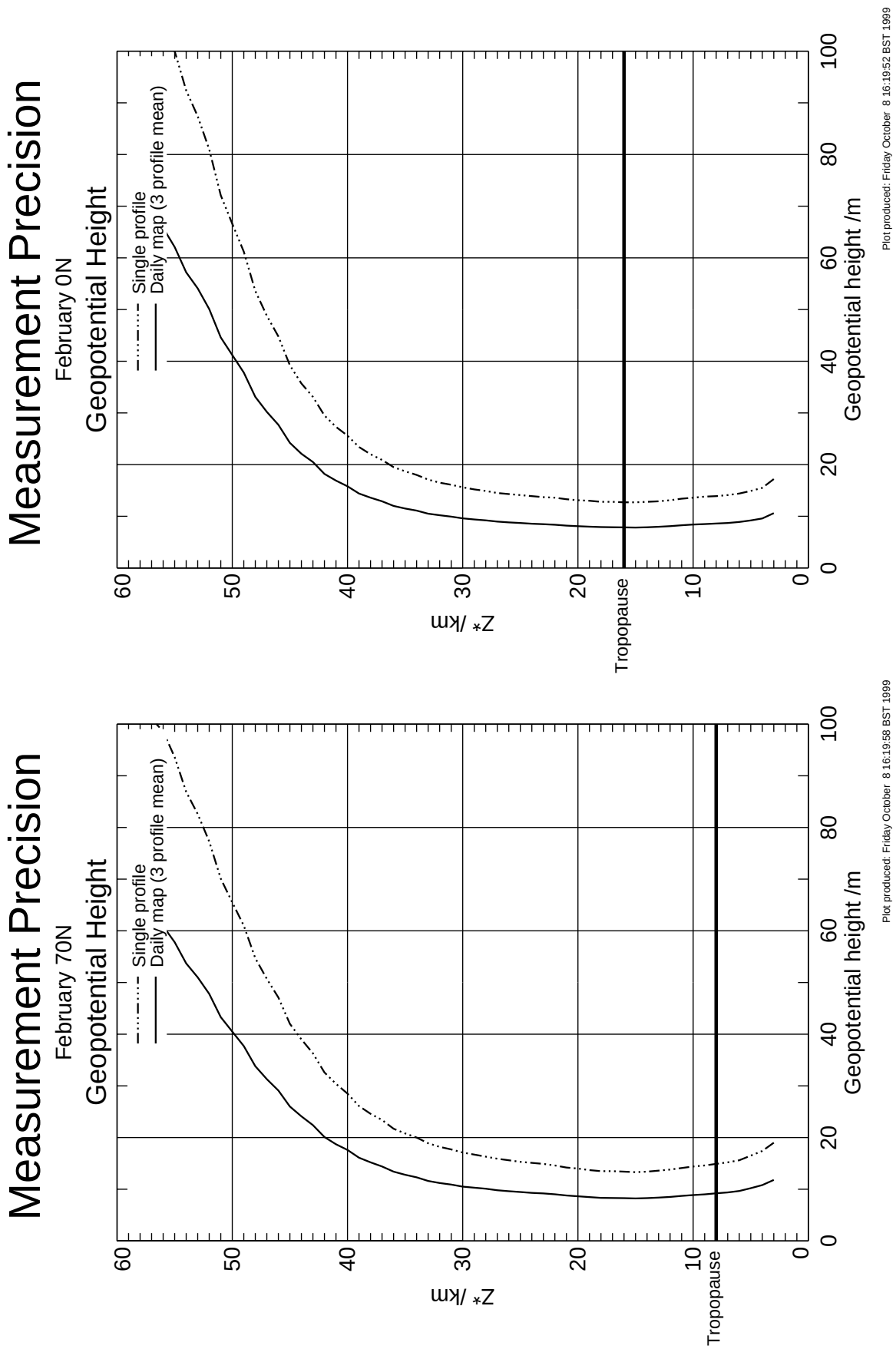

Figure 6: Geopotential height precision based on 3 km vertical resolution for temperature, for Single Profiles and Daily Map only.

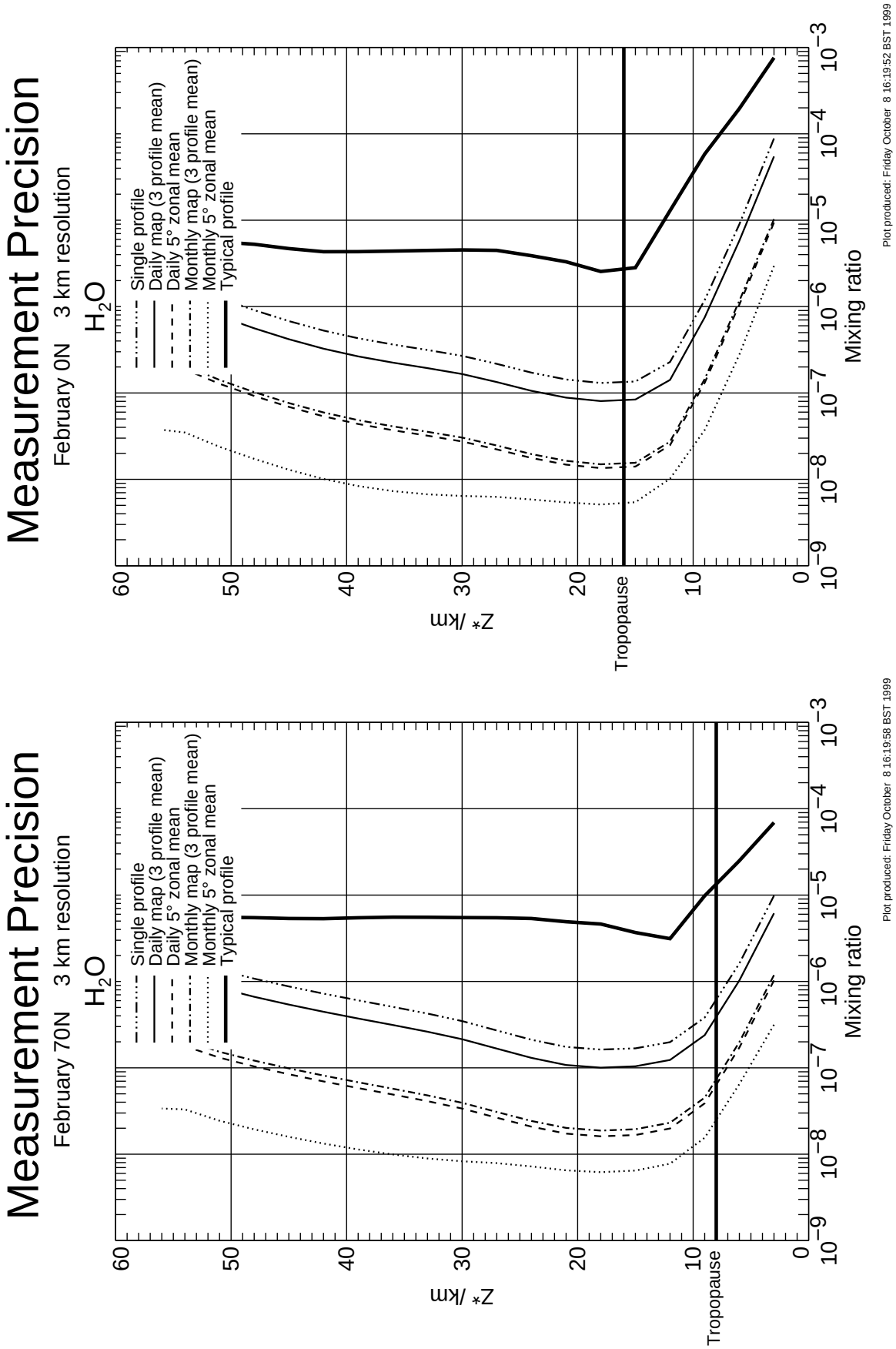

Figure 7: H_2O precision at 3 km vertical resolution, for varying space/time averages.

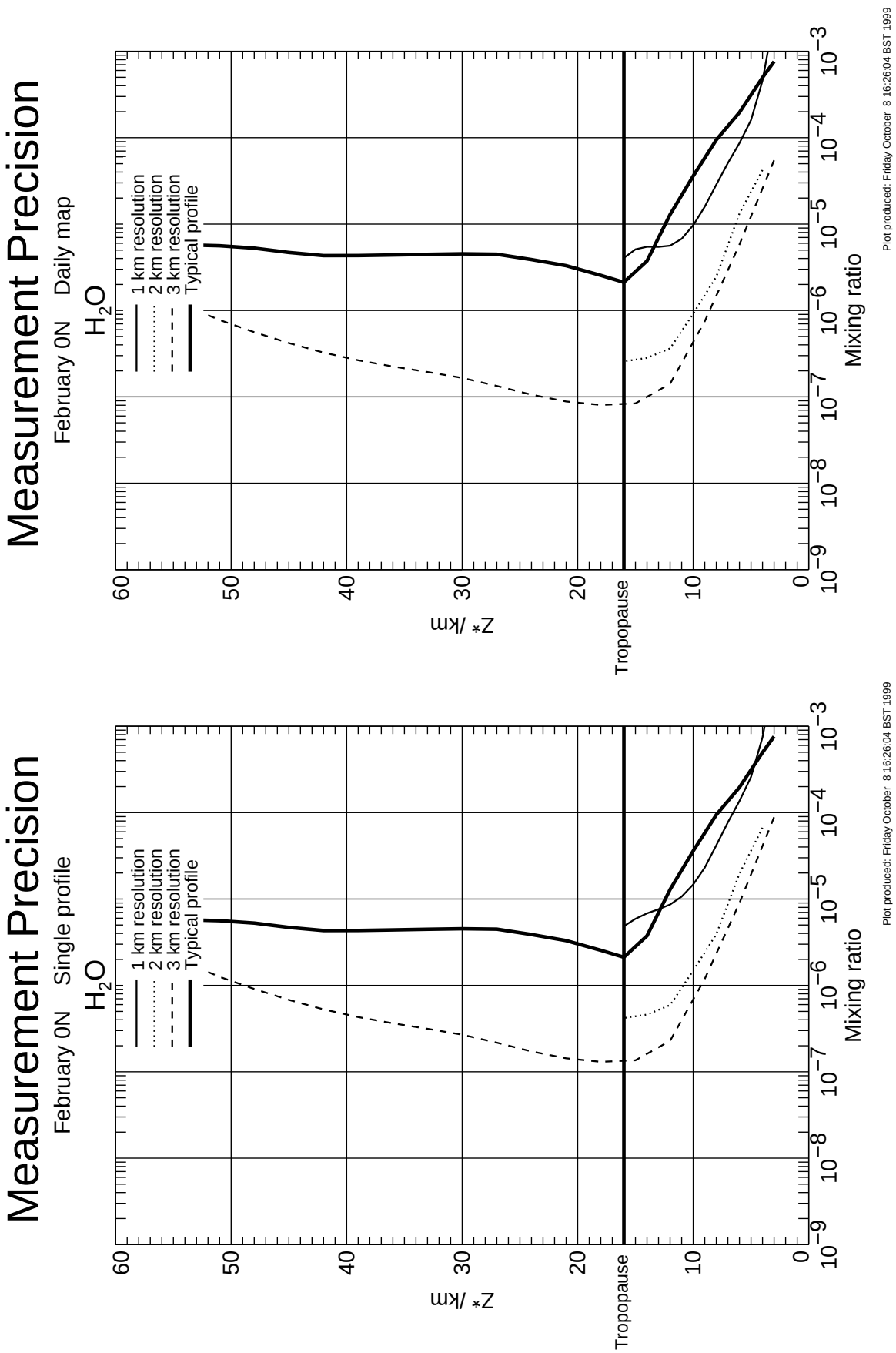

Figure 8: H_2O precision at 1, 2, 3 km vertical resolution in the troposphere, for Single Profile and Daily Map (February Equator only). The resolution in the stratosphere remains 3 km.

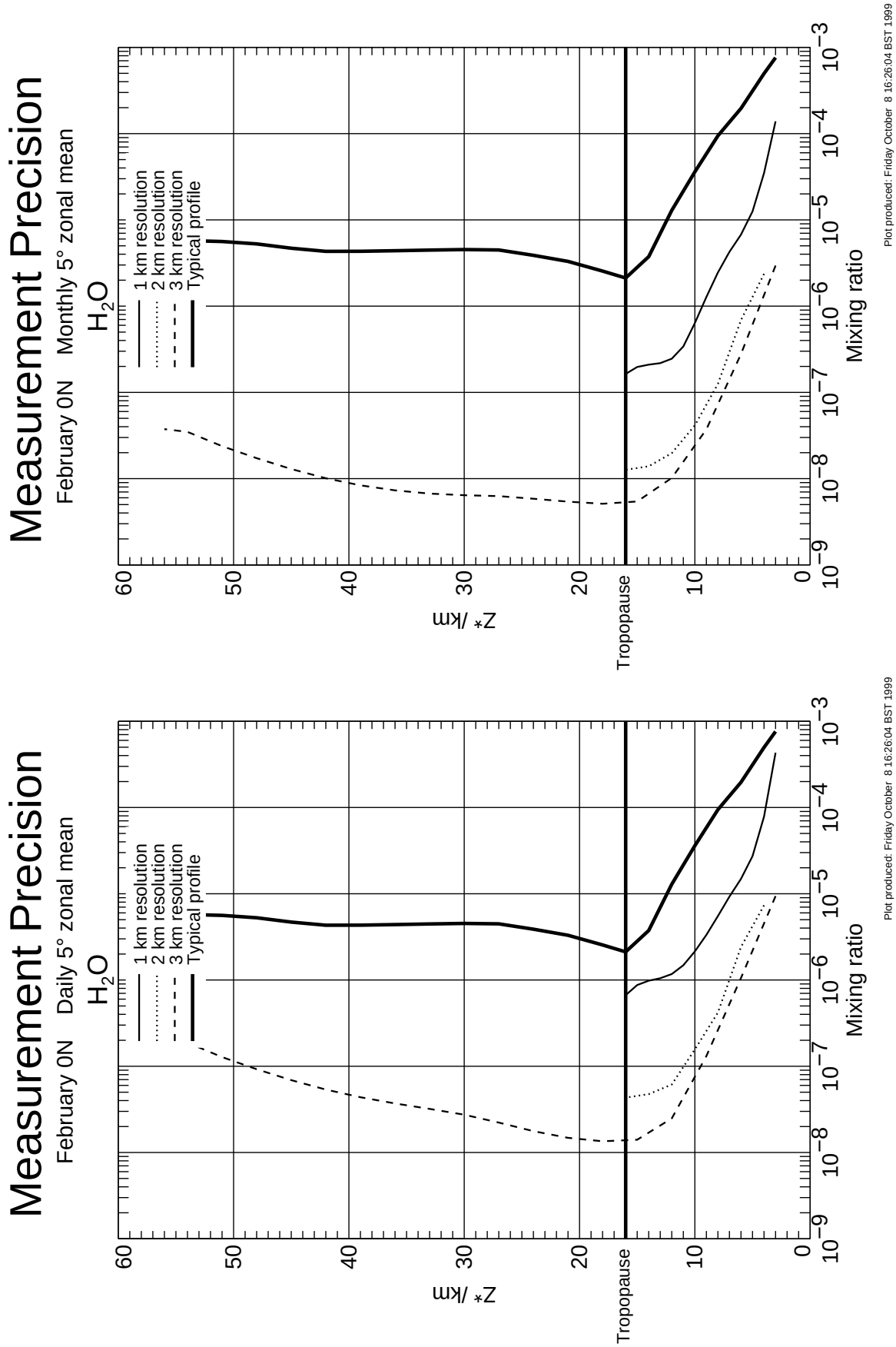

Figure 9: H_2O precision at 1, 2, 3 km vertical resolution in the troposphere, for Daily Zonal Mean and Monthly Zonal Mean (February Equator only). The resolution in the stratosphere remains 3 km.

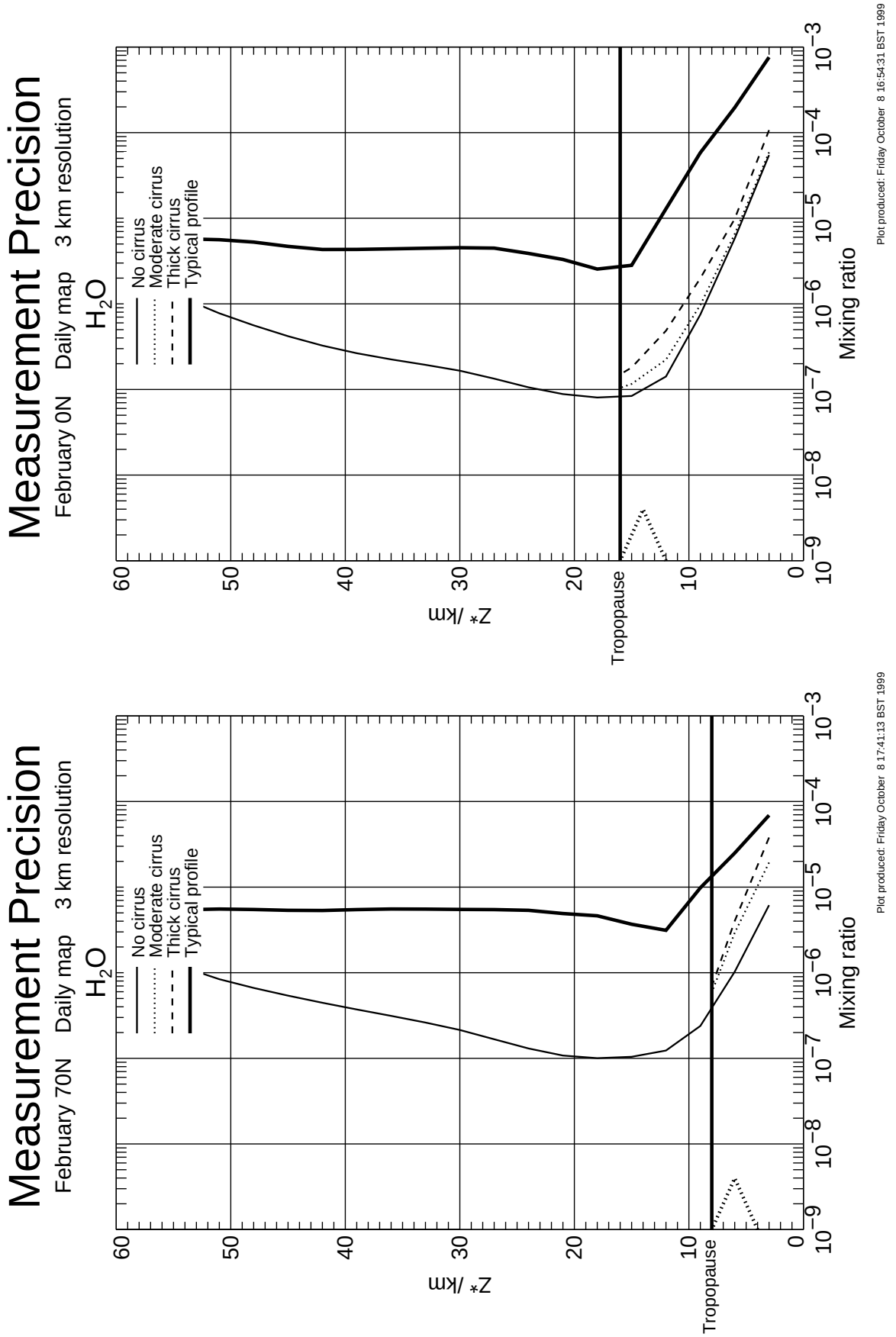

Figure 10: The effect of cirrus clouds (without scattering) on H_2O precision in the troposphere, for Daily Map only. The vertical resolution is 3 km. On the left of each plot is an indication of the position and shape of the cirrus cloud. Moderate cirrus has IWC=0.05 g m^{-3}, thick cirrus has IWC=0.5 g m^{-3}.

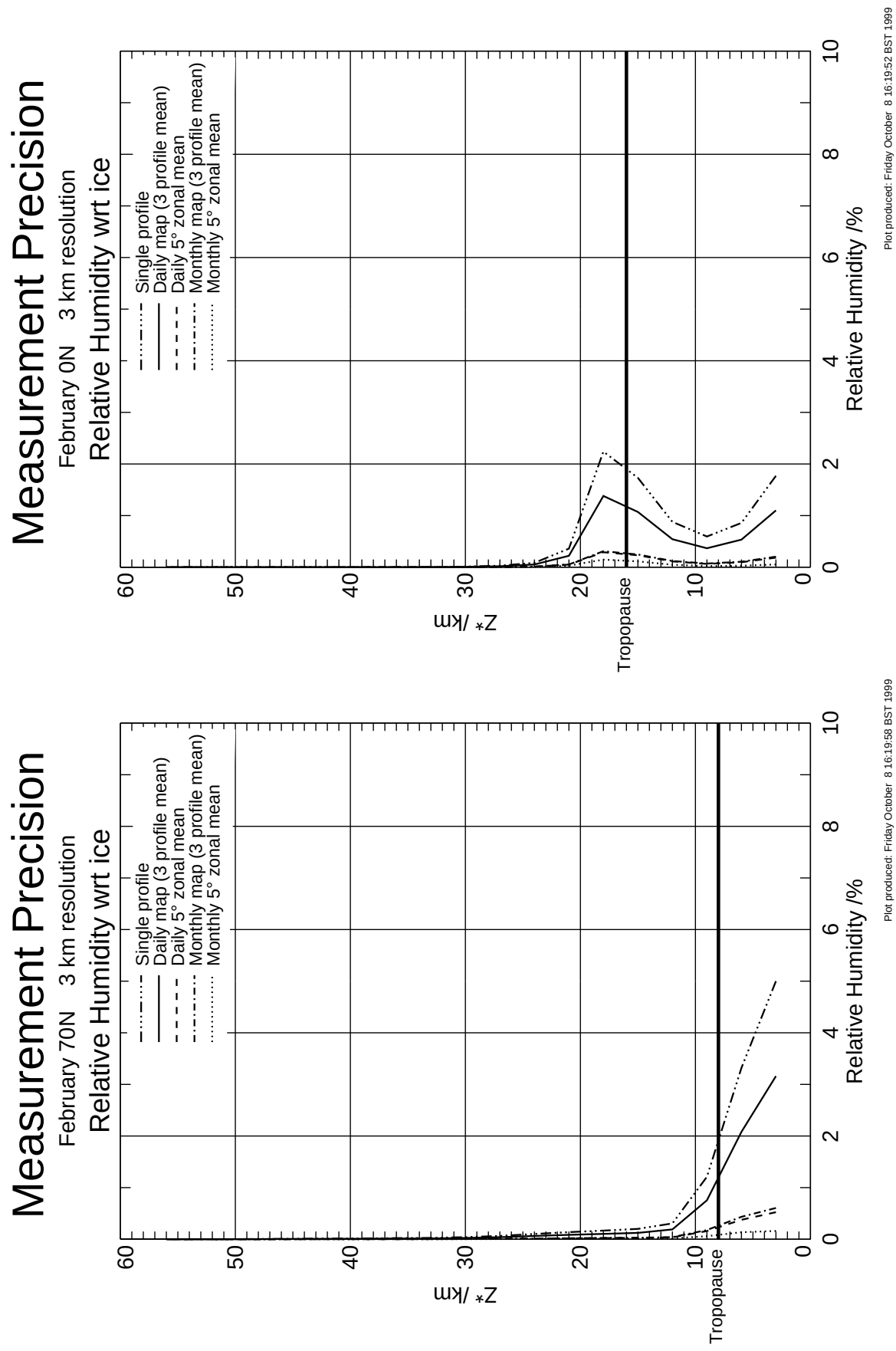

Figure 11: Relative humidity precision at 3 km vertical resolution, for varying space/time averages. Tropospheric relative humidity is highly variable, both temporally and spatially (vertically and horizontally), and can have values from near zero to somewhat more than 100%. In the tropics near 150 hPa (~14 km), for example, a fairly flat distribution of relative humidities between ~10% and ~100% is observed (Sandor *et al.* 1998).

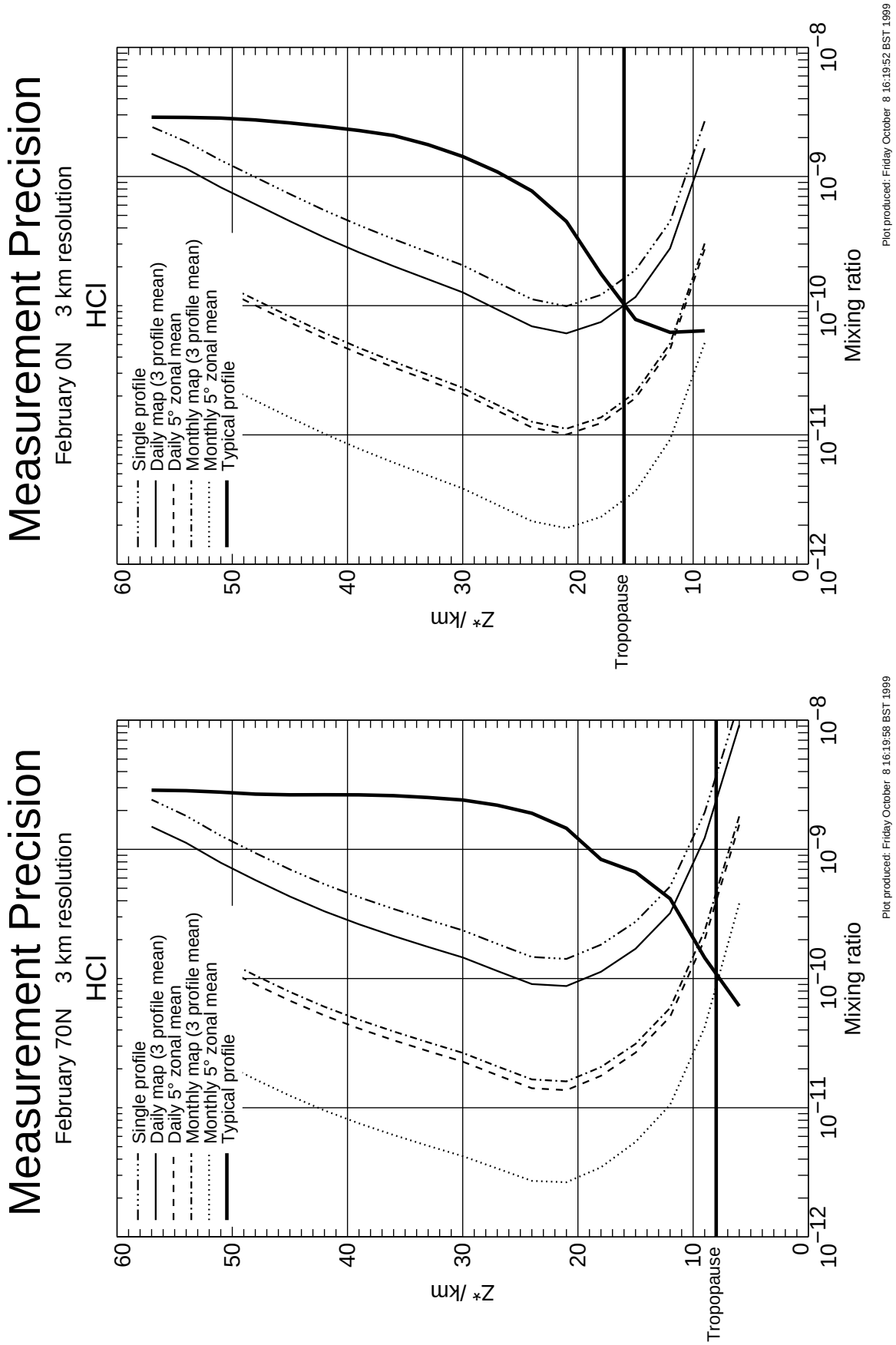

Figure 12: HCl precision at 3 km vertical resolution, for varying space/time averages.

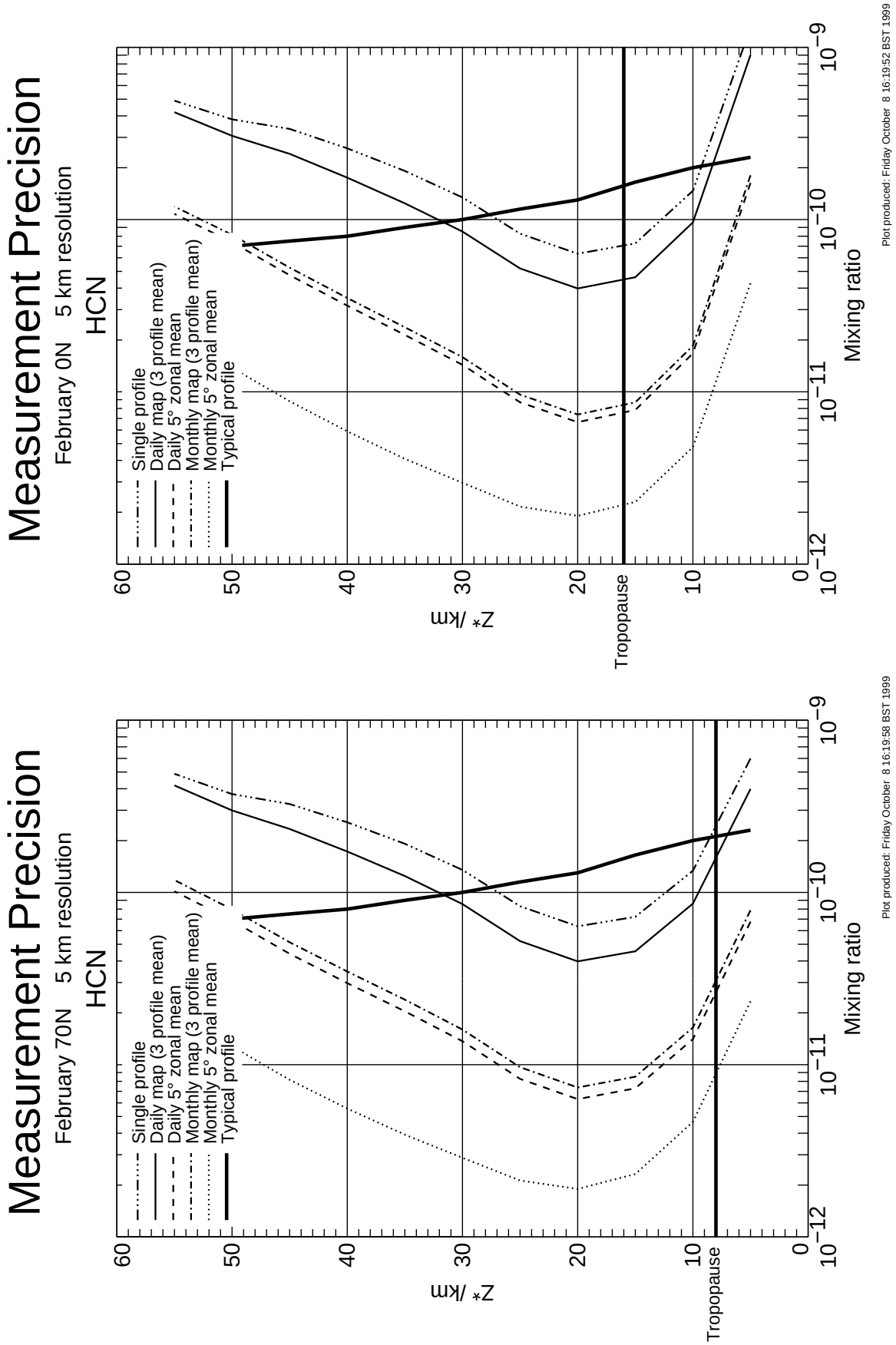

Figure 13: HCN precision at 5 km vertical resolution, for varying space/time averages.

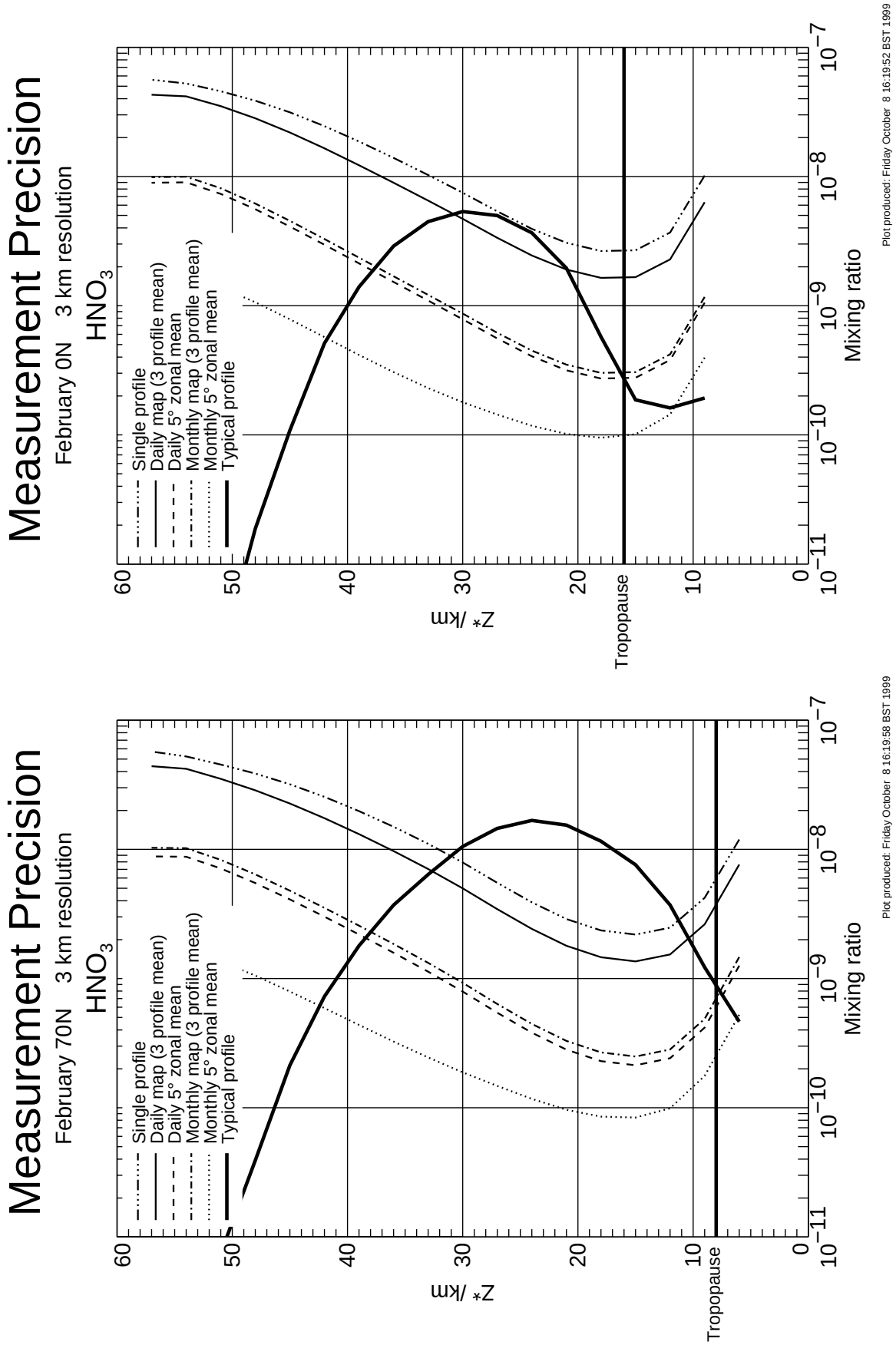

Figure 14: HNO_3 precision at 3 km vertical resolution, for varying space/time averages.

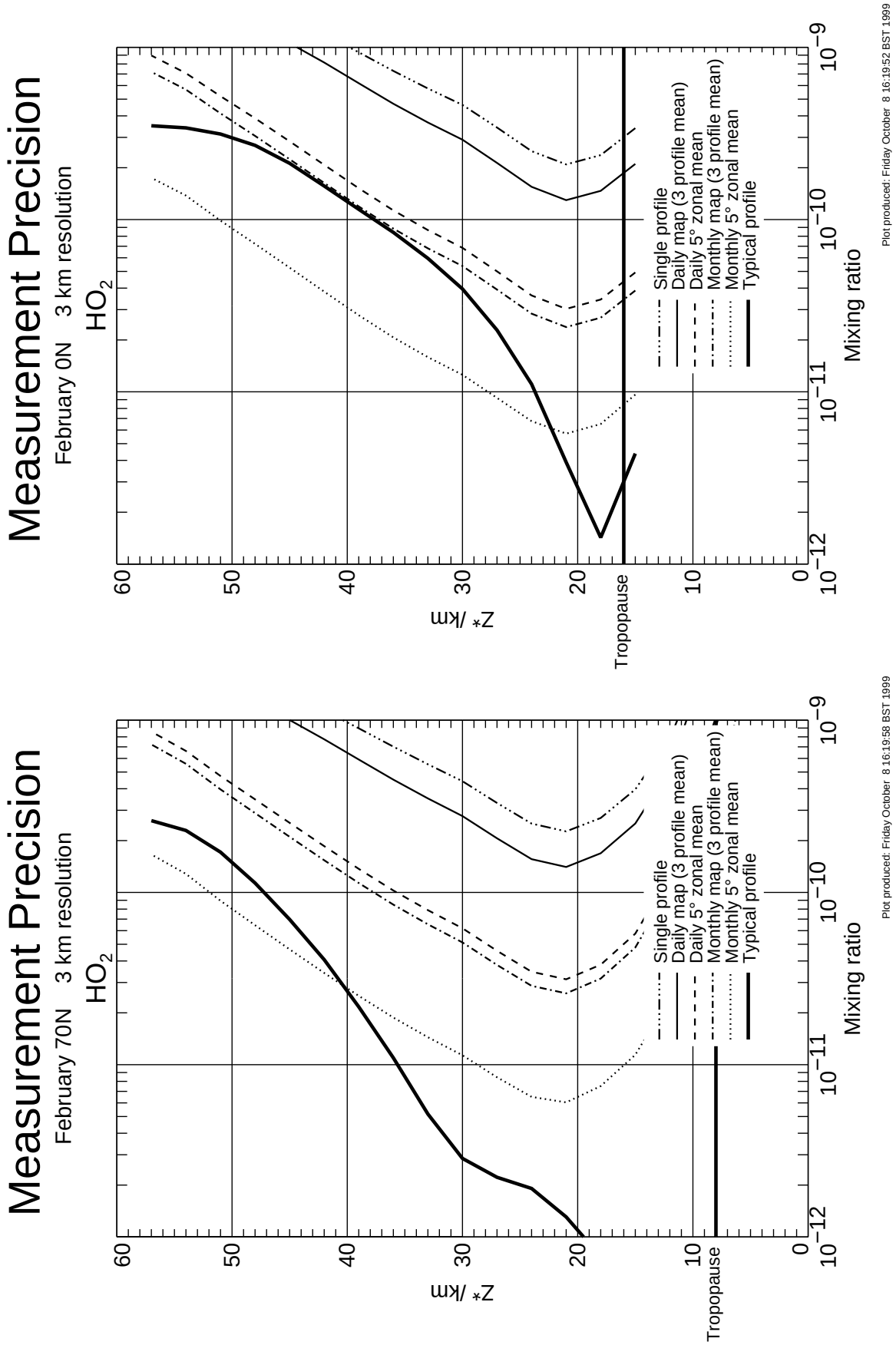

Figure 15: HO_2 precision at 3 km vertical resolution, for varying space/time averages.

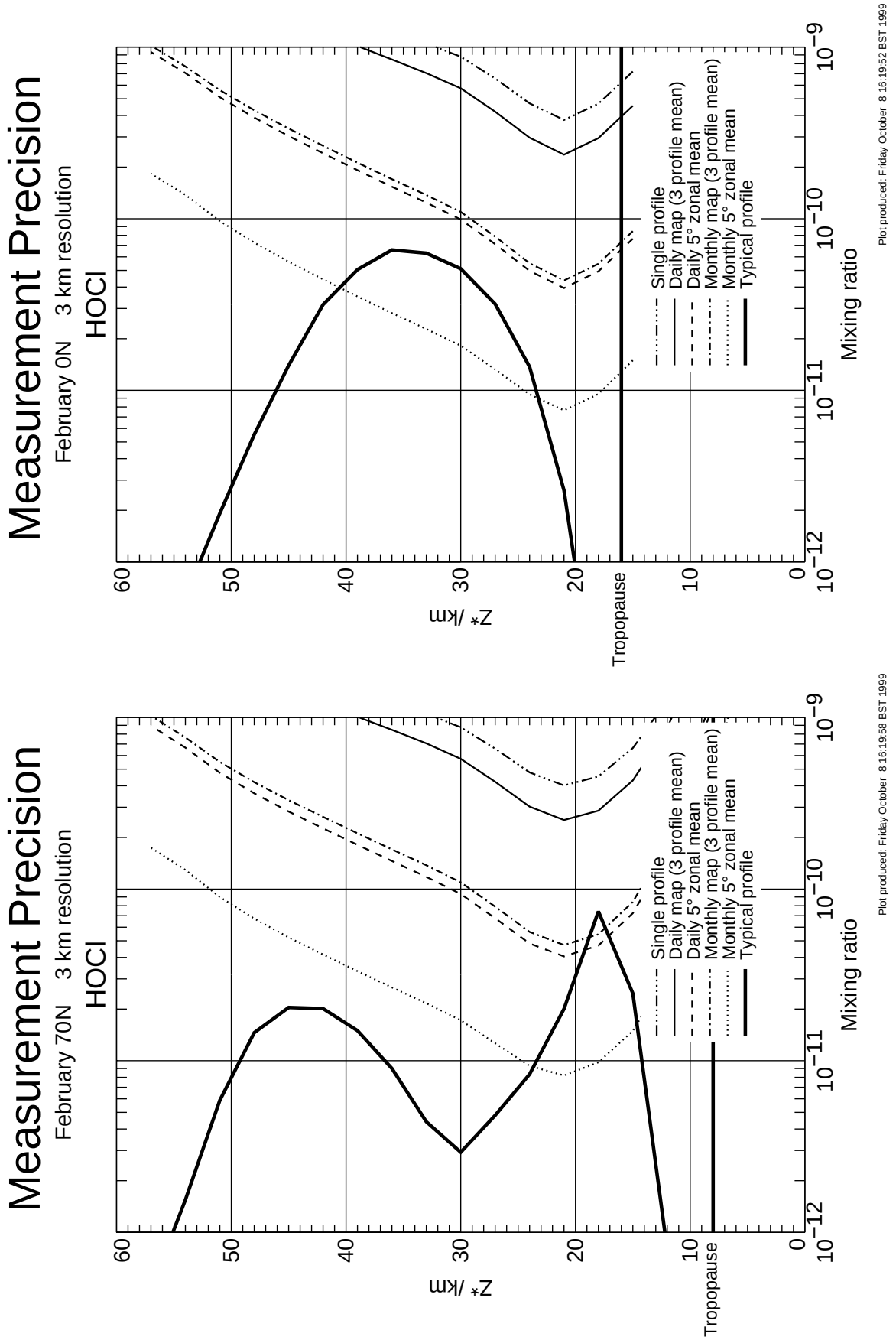

Figure 16: HOCl precision at 3 km vertical resolution, for varying space/time averages.

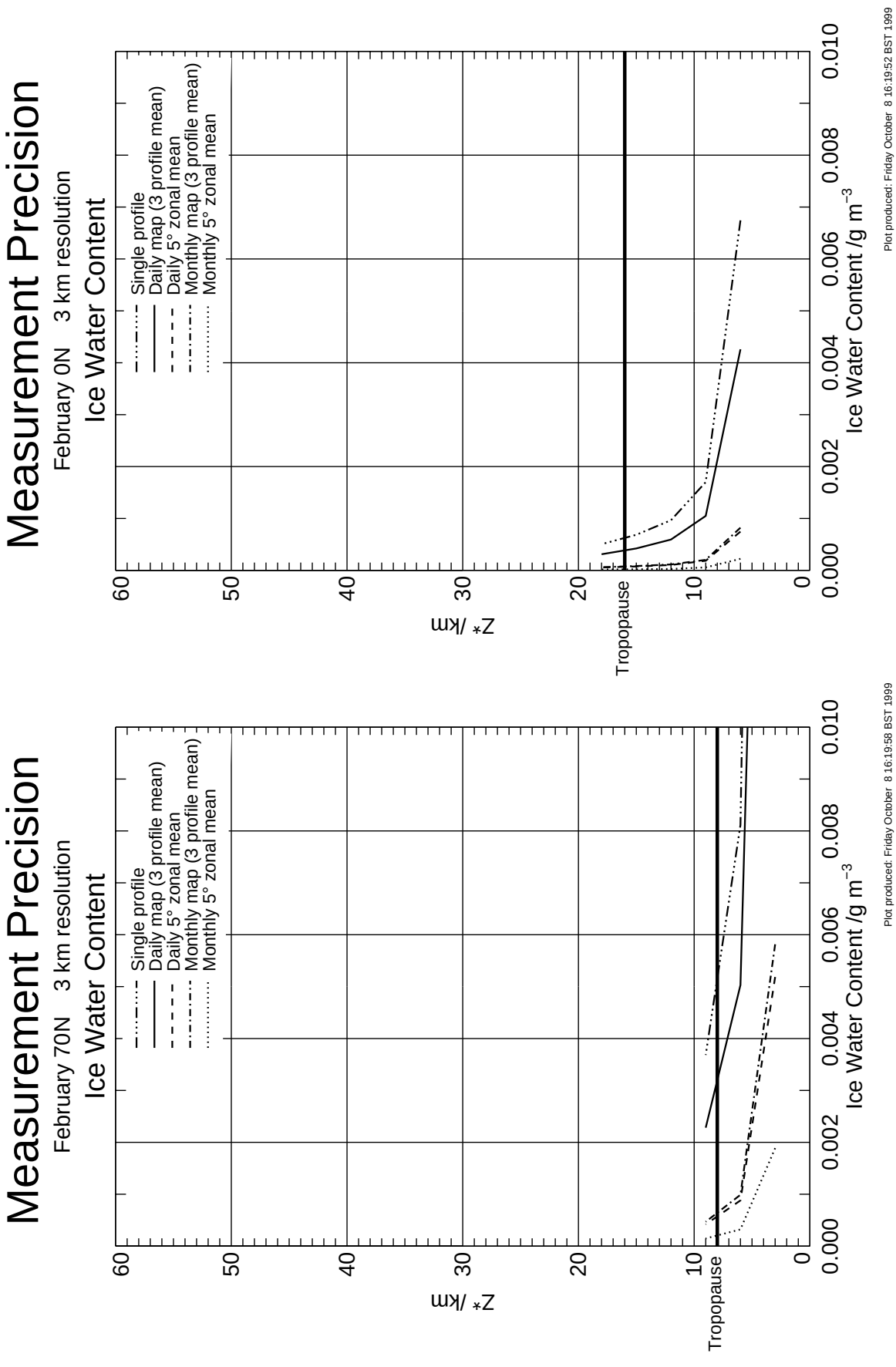

Figure 17: Ice water content precision at 3 km vertical resolution, for varying space/time averages. Moderate cirrus has IWC=0.05 g m^{-3}, thick cirrus has IWC=0.5 g m^{-3}. Note that these estimates are based on simulations using cirrus with IWC=0.01 g m^{-3}.

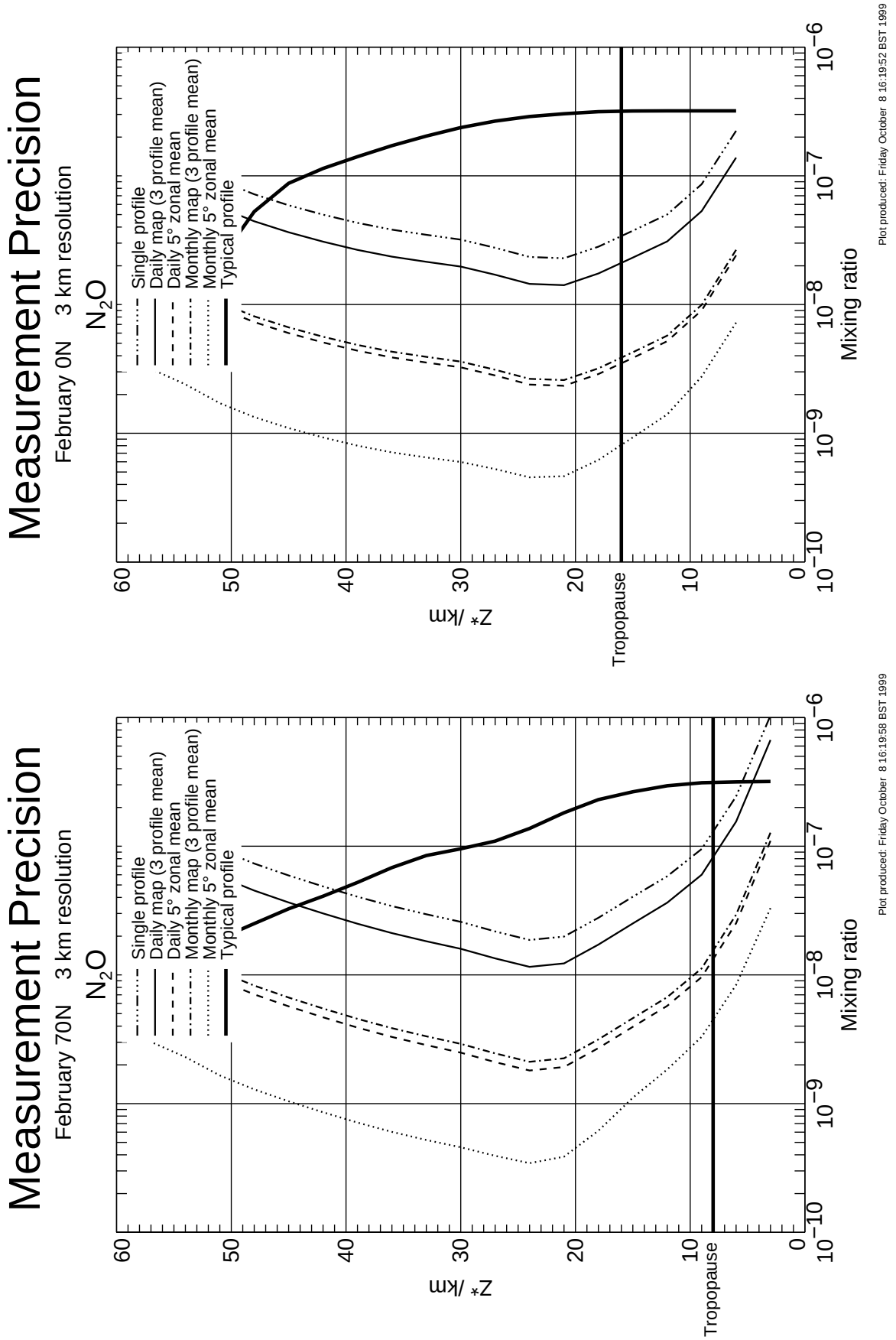

Figure 18: N_2O precision at 3 km vertical resolution, for varying space/time averages.

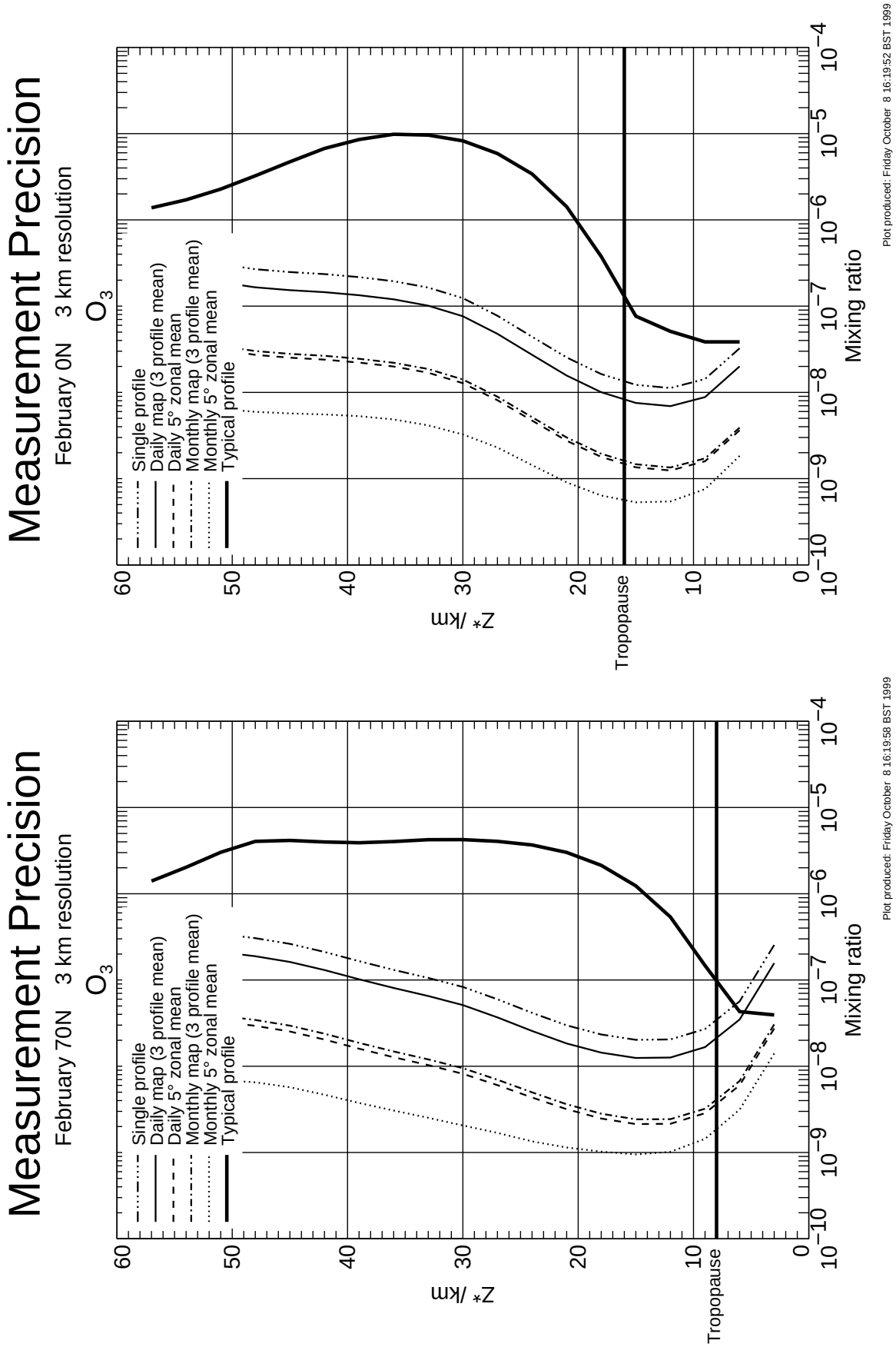

Figure 19: O_3 precision at 3 km vertical resolution, for varying space/time averages.

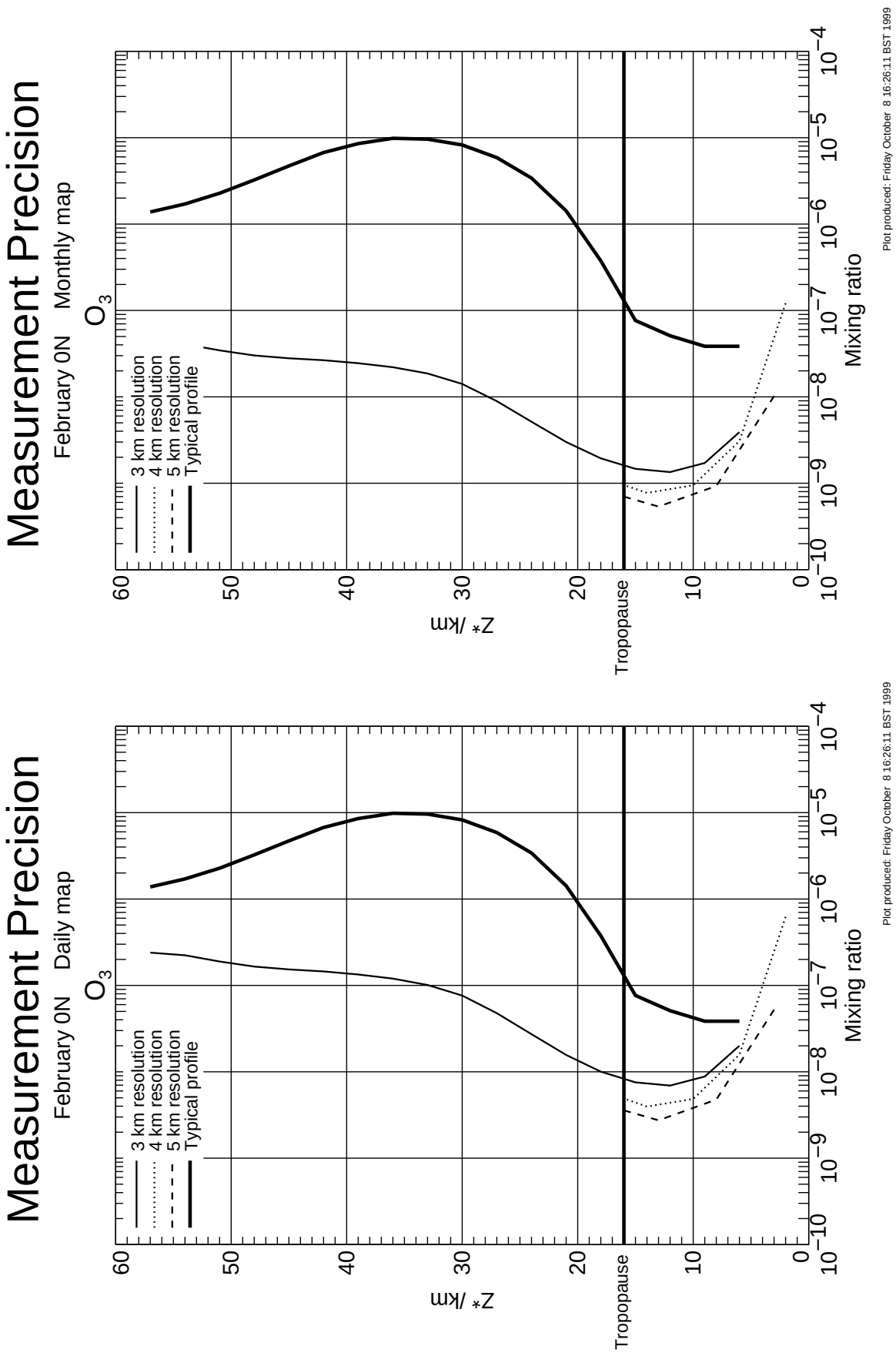

Figure 20: O_3 precision at 3, 4, 5 km vertical resolution in the troposphere, for Daily Map and Monthly Map (February Equator only). The resolution in the stratosphere remains 3 km.

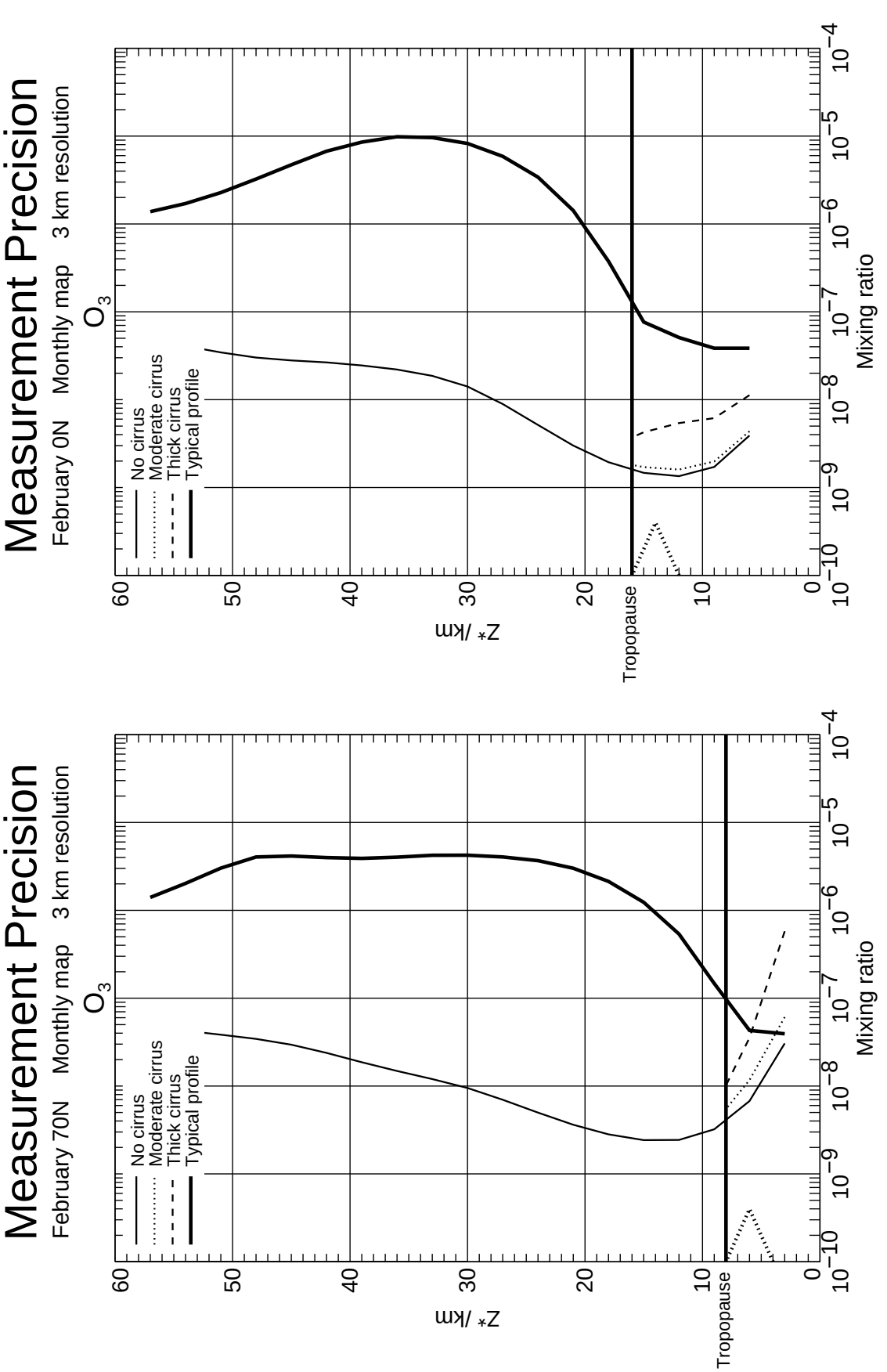

Figure 21: The effect of cirrus clouds (without scattering) on O_3 precision in the troposphere, for Monthly Map only. The vertical resolution is 3 km. On the left of each plot is an indication of the position and shape of the cirrus cloud. Moderate cirrus has IWC=0.05 g m^{-3}, thick cirrus has IWC=0.5 g m^{-3}.

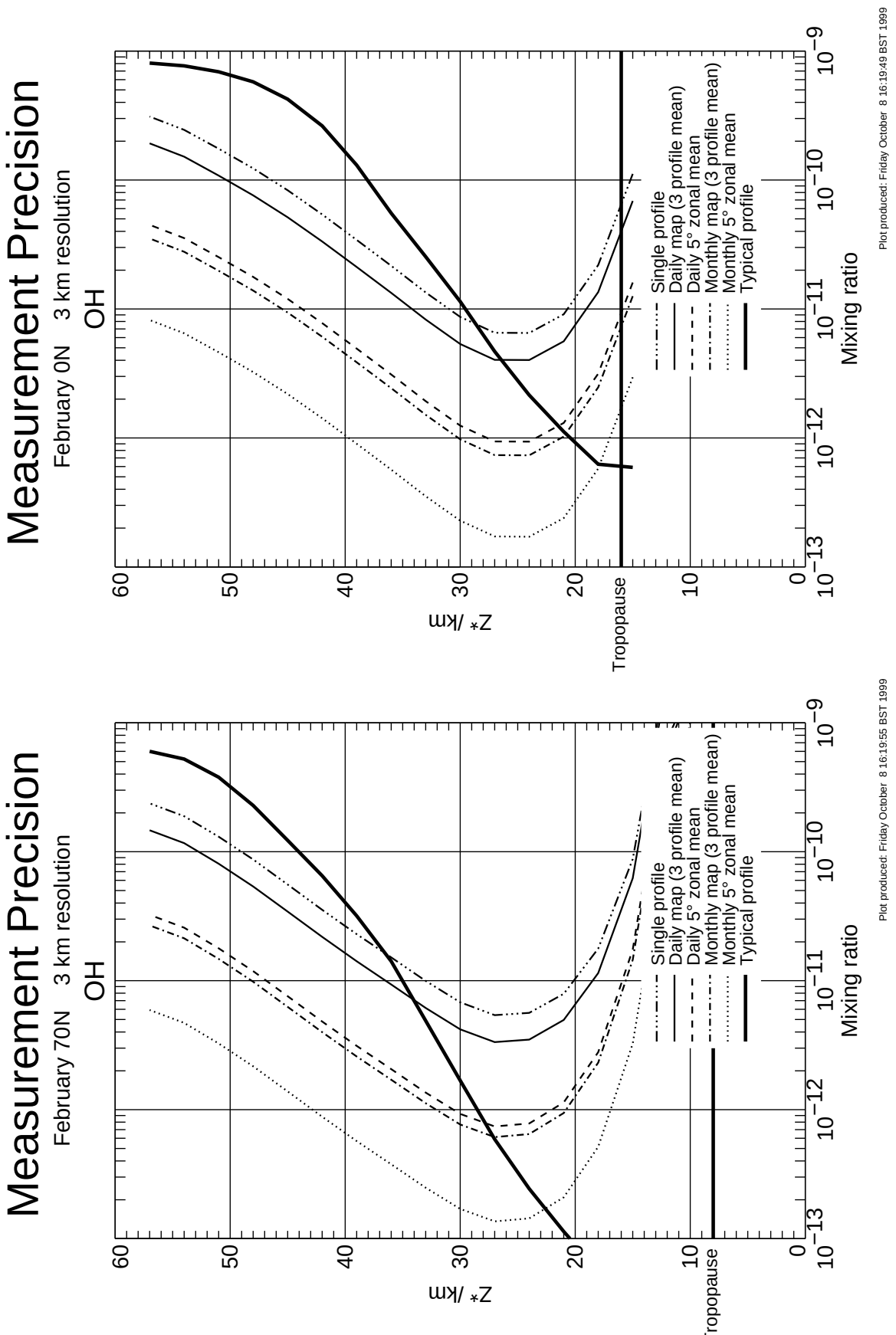

Figure 22: OH precision at 3 km vertical resolution, for varying space/time averages. The OH profile is a daylight average. These estimates agree closely with independent simulations by H.M. Pickett.

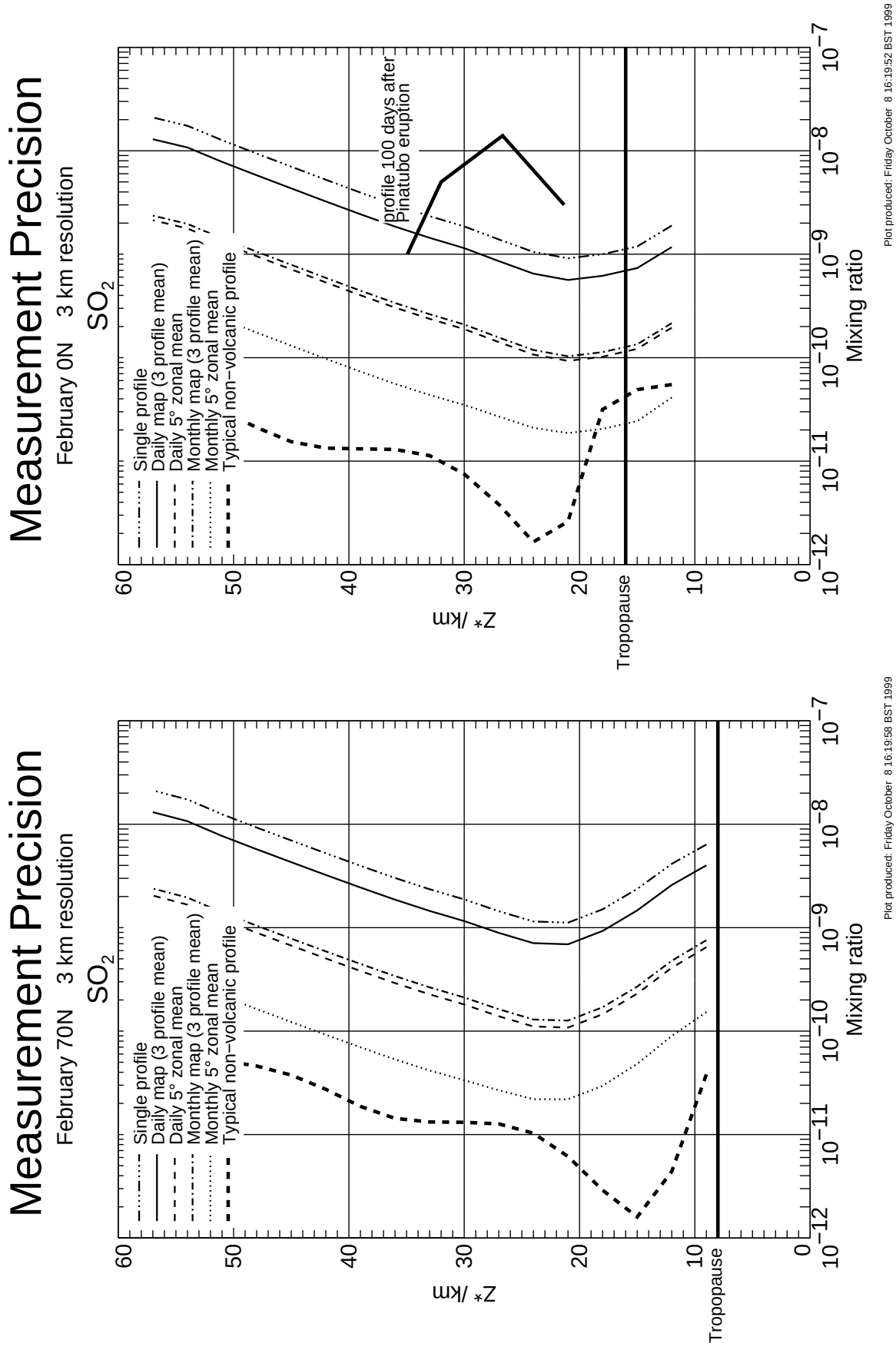

Figure 23: SO_2 precision at 3 km vertical resolution, for varying space/time averages. The enhanced SO_2 profile comes from an average of UARS MLS measurements in the latitude band 10°S–0° for 21 September 1991, ~100 days after the Mt. Pinatubo eruption (Read *et al.* 1993).

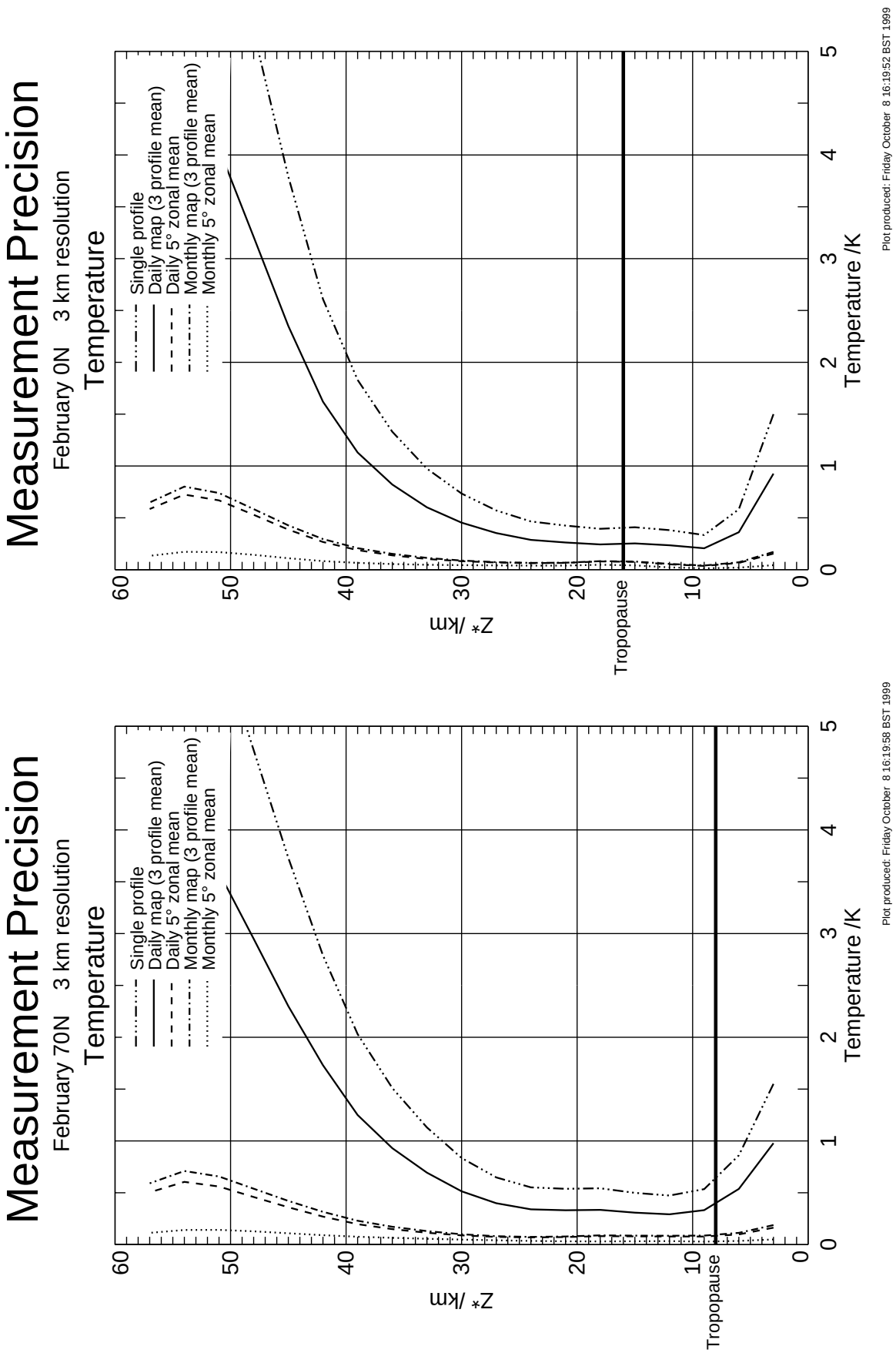

Figure 24: Temperature precision at 3 km vertical resolution, for varying space/time averages.

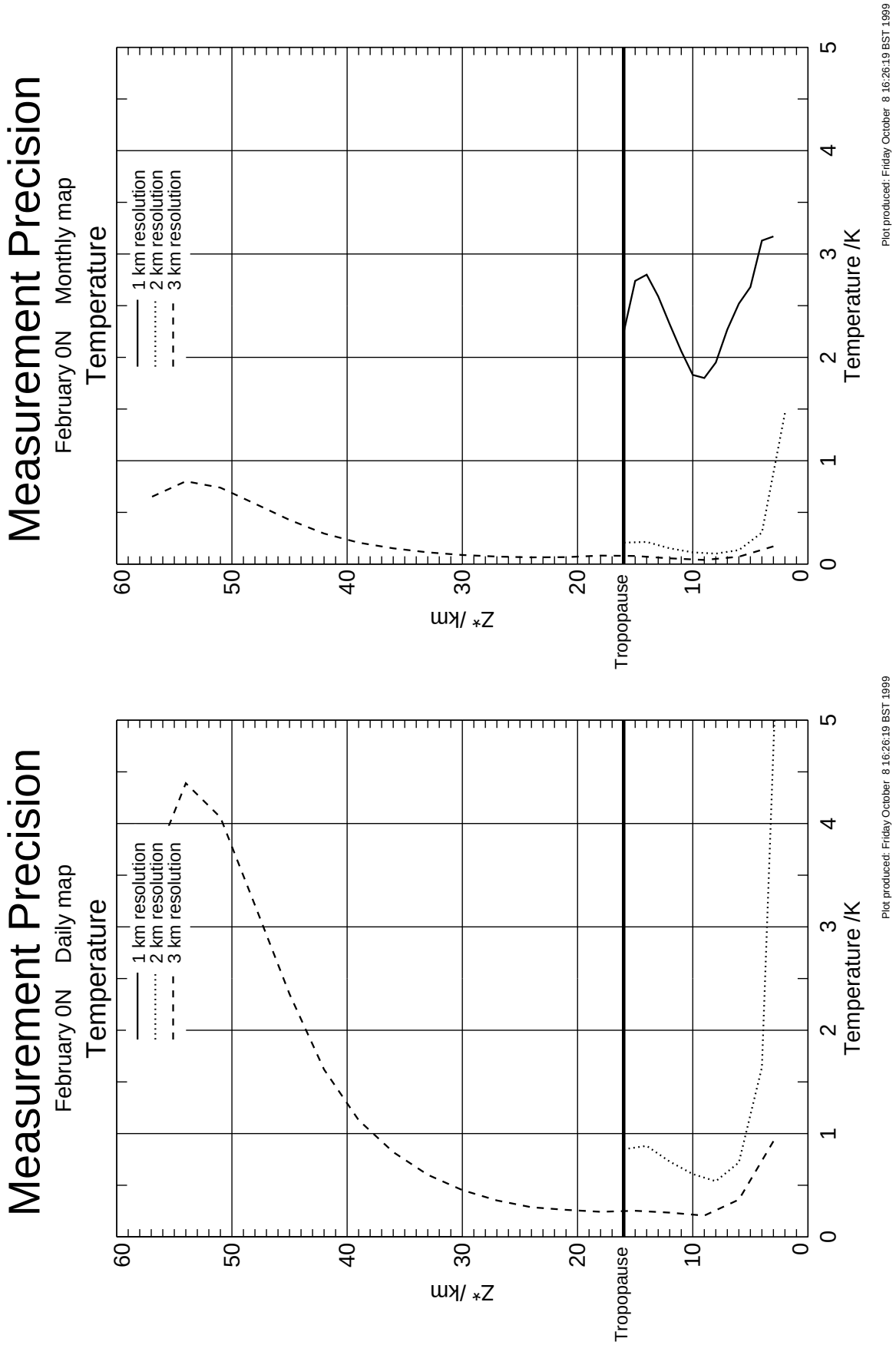

Figure 25: Temperature precision at 1, 2, 3 km vertical resolution in the troposphere, for Daily Map and Monthly Map (February Equator only). The resolution in the stratosphere remains 3 km. This figure illustrates that EOS MLS can produce daily maps of temperature in the upper tropical troposphere to better than 1 K, with 2 km vertical resolution.

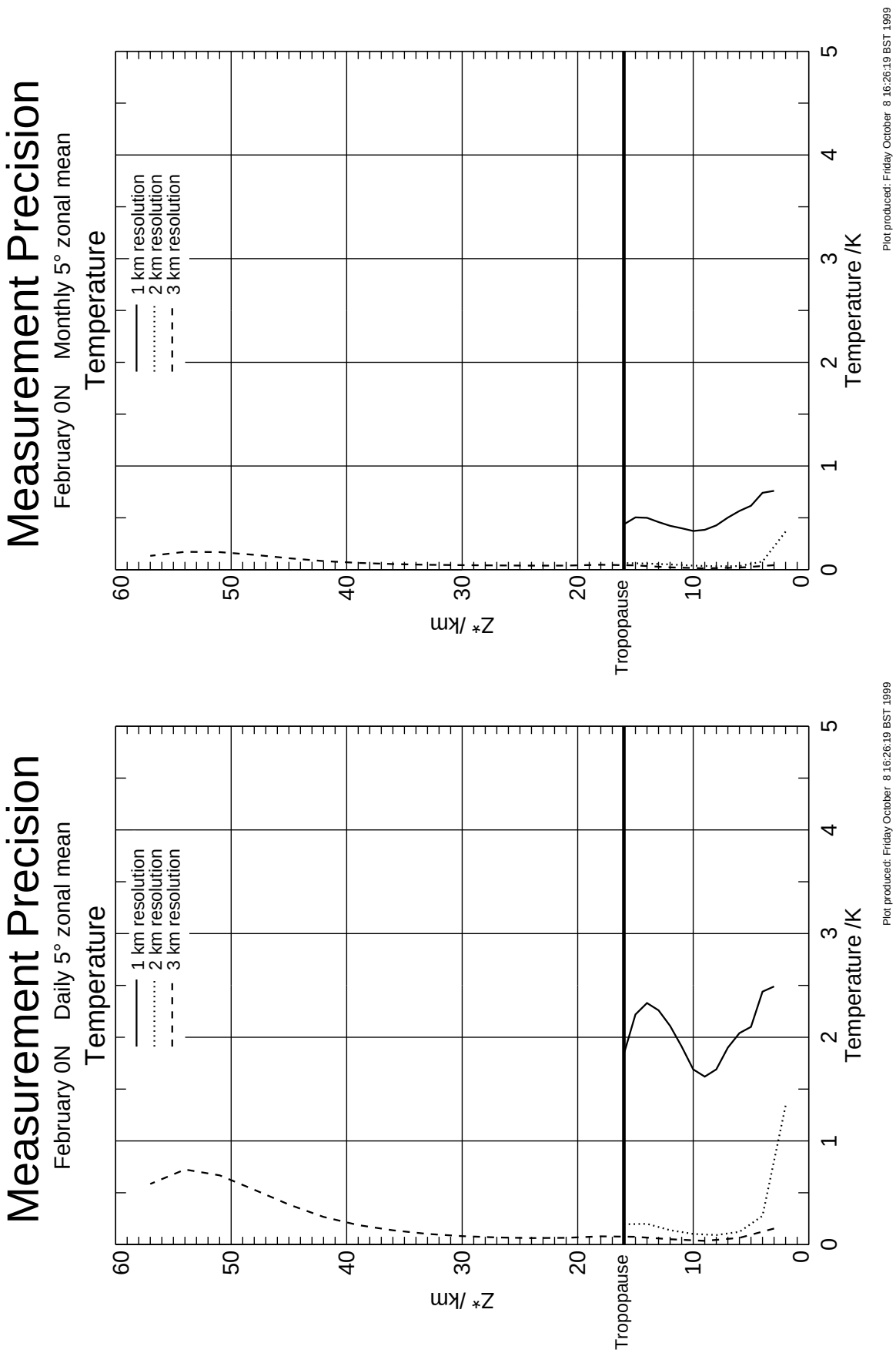

Figure 26: Temperature precision at 1, 2, 3 km vertical resolution in the troposphere, for Daily Zonal Mean and Month Zonal Mean (February Equator only). The resolution in the stratosphere remains 3 km.

5 Resolution of H_2O and temperature in the troposphere

The grid resolution of the H_2O and temperature measurements in the troposphere can be as fine as 1–2 km: for H_2O, the Daily Map precision is ∼30% for 1 km grid resolution, and for temperature the Daily Map precision is ∼0.5 K for 2 km grid resolution.

The high resolution in the troposphere can be seen more clearly by plotting the averaging kernels for H_2O and temperature (see Figures 27–28). These were generated using Equation 6 for the averaging kernel matrix **A**, using a 0.5 km* grid for H_2O or temperature, and the 'standard' resolution for the other measurements. The averaging kernels plotted are from the diagonal blocks of **A** corresponding to H_2O or temperature.

The line-style for the averaging kernels cycles to separate them visually, but has no other significance. The peak of each averaging kernel is labelled with the measurement height (which may not correspond to the peak height). The *a priori* was chosen to approximate the precision achieved in the troposphere for 1–2 km grid resolution, and is given in Table 2.

The full width at half maximum gives a good estimate of the grid resolution. In the troposphere H_2O is measured with a resolution of ∼1.5 km in a Daily Map and ∼1 km in a Daily Zonal Mean; temperature is measured with a resolution of ∼2.5 km in a Daily Map and ∼1.5 km in a Daily Zonal Mean. These values confirm that, even accounting for these values being for the grid resolution, rather than based on the highest representable spatial frequency, the resolution can exceed that expected from the FOV width of the EOS MLS antenna (see Table 5-4 of Waters (1999)). A major contributor to the good tropospheric resolution is the strong vertical gradient of H_2O in the troposphere. The channels in the 191.9 GHz radiometer (other radiometers will have some contribution as well) have sufficient range and frequency resolution that EOS MLS can act as a 'nadir' sounder. Since the channels saturate at different H_2O mixing ratios (effectively), it is the H_2O scale height (about 2 km), rather than the pressure scale height, that sets the achievable resolution. For the H_2O measurement, this effect becomes important below ∼13 km (see Figure 27); for the temperature measurement, below ∼11 km (see Figure 28).

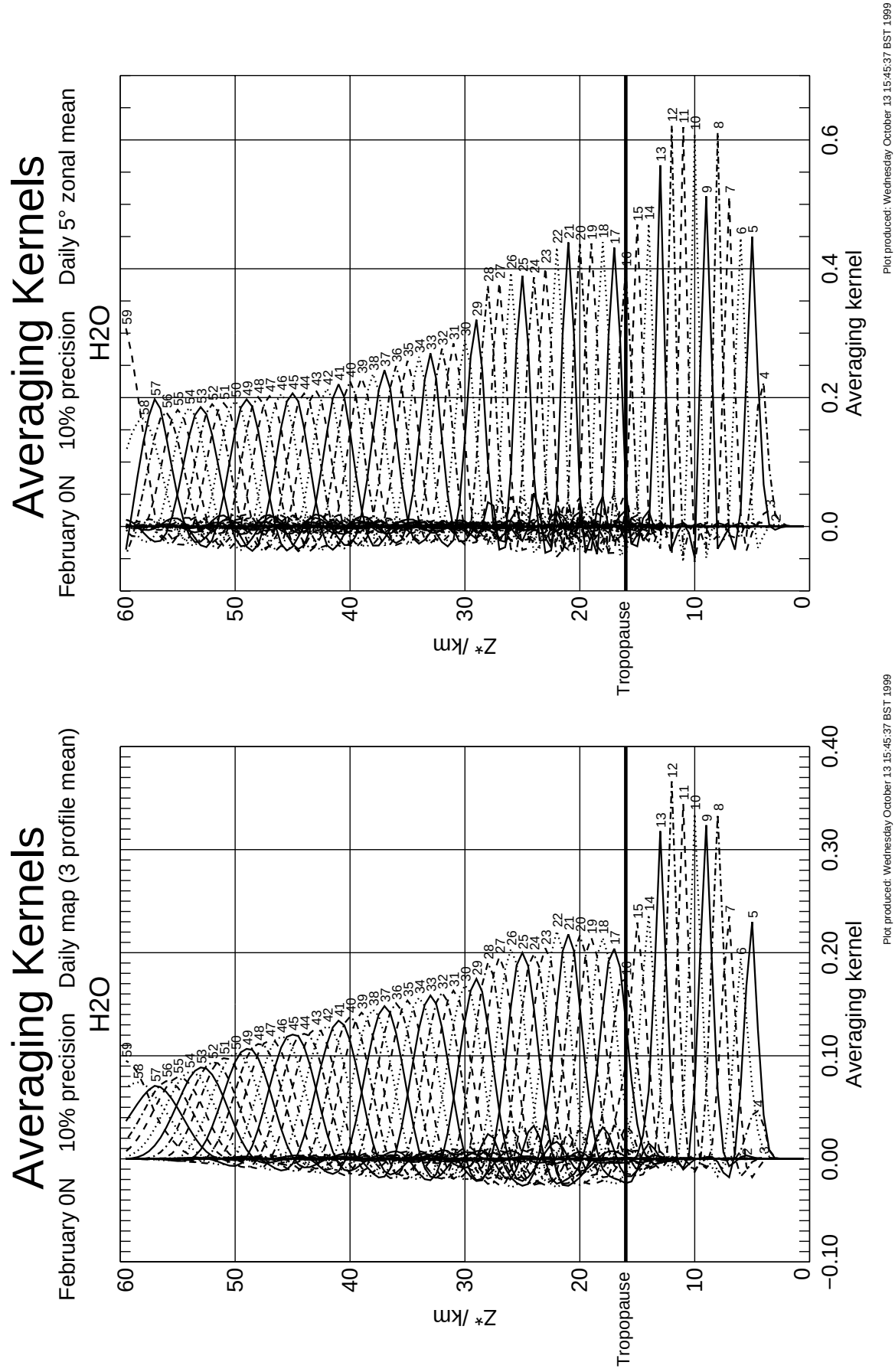

Figure 27: H_2O averaging kernels at ~10% precision for Daily Map and Daily Zonal Mean (February Equator only). The line style for the averaging kernels is cycled through 4 patterns to help differentiate them, and each averaging kernel is labelled with its measurement height (in km*). The full width at half maximum of the averaging kernel peak is a measure of the vertical resolution: in the troposphere this is ~1.5 km in the Daily Map, and ~1 km in the Daily Zonal Mean.

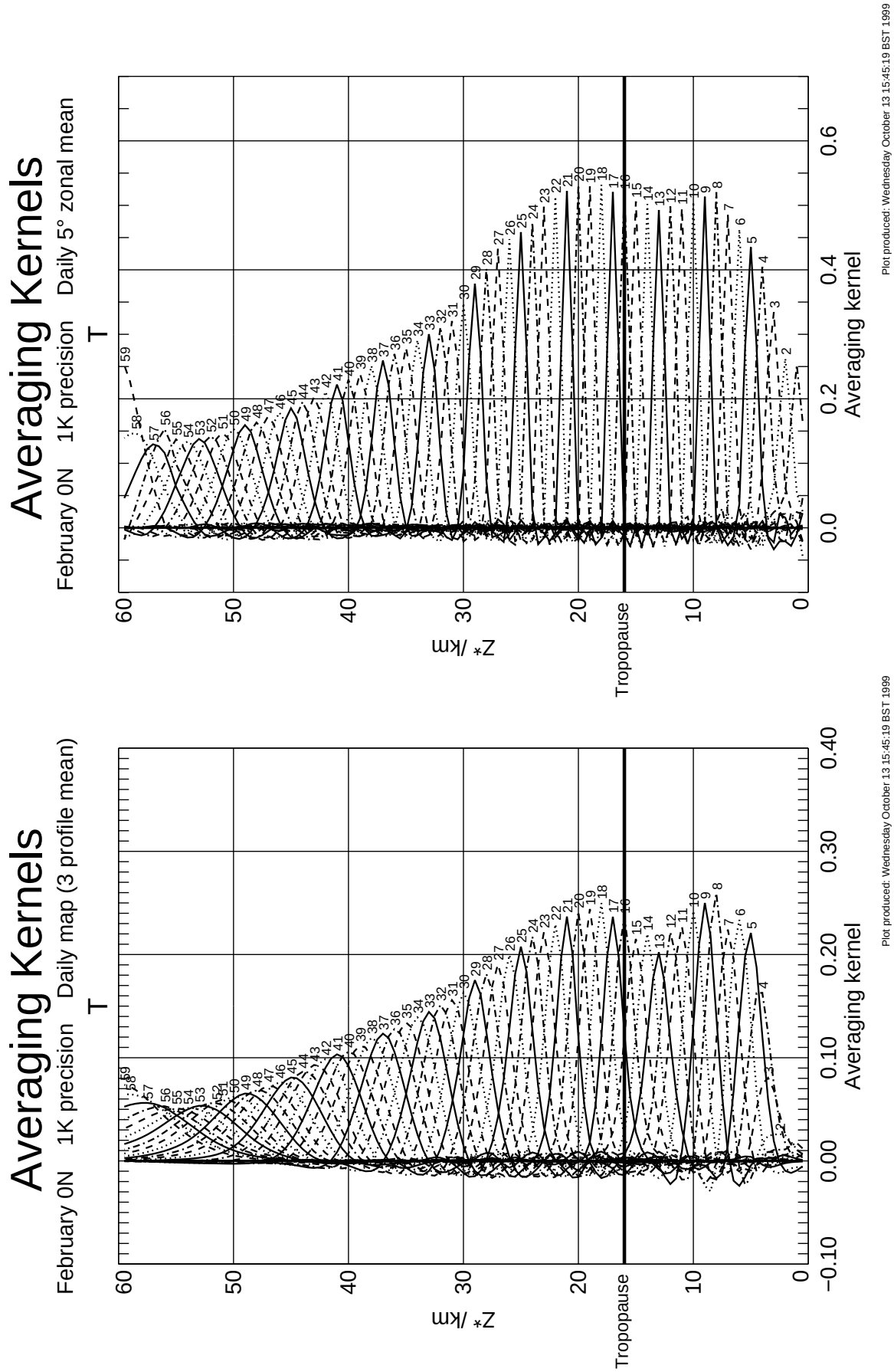

Figure 28: Temperature averaging kernels at ~1 K precision for Daily Map and Daily Zonal Mean (February Equator only). The line style for the averaging kernels is cycled through 4 patterns to help differentiate them, and each averaging kernel is labelled with its measurement height (in km*). The full width at half maximum of the averaging kernel peak is a measure of the vertical resolution: in the troposphere this is ~2.5 km in the Daily Map, and ~1.5 km in the Daily Zonal Mean.

6 Comparison of simulations with scaled UARS MLS results

For optically-thin spectral lines, it is possible to estimate precision for EOS MLS products by scaling from precisions achieved by UARS MLS. This scaling estimate can be compared with the simulation results to (partially) validate the simulation.

Table 4 shows the scalings and comparisons which have been calculated by J.W. Waters and updated with the most recent simulation results. The scaling is with reference to the UARS MLS 206 GHz O_3 measurement and takes into account

- The ratio of radiometer noise to UARS MLS 206 GHz O_3 radiometer noise,
- the ratio of linestrength to the UARS MLS 206 GHz O_3 linestrength,
- the combination of measurements in EOS MLS (e.g. ClO is measured in two radiometers), and
- isotopic abundances.

The formula for the scaled precision is

$$\text{(scaled precision)} = \text{(reference precision)} * \text{(radiometer noise ratio)}/\text{(linestrength ratio)}.$$

The calculations and simulations are for optically thin lines at 22 hPa ($\sim$27 km*). The vertical resolution in the simulations is set at 3 km* except for HNO_3 and HCN, set at 4 km* to match the EOS MLS FOV width at 180 GHz. The daily map space/time average is used. This combination of space and time resolution matches the effective integration time for the UARS MLS measurements.

Table 4: EOS precisions obtained by scaling from UARS MLS (calculated by J.W. Waters) compared with precisions obtained from simulations.
* indicates spectral line has fine structure. (H) and (V) indicate the two polarizations measured for OH.

UARS or EOS MLS	molecule	line frequency (GHz)	line strength at T=225K (JPL catalog units)	radiometer noise temperature (K, SSB)	line strength ratio	radiometer noise ratio	scaled precision for single line (mixing ratio)	scaled precision for combined lines (mixing ratio)	scaled precision adjusted to total isotopic abundance (mixing ratio)	precision from simulations for EOS or achieved on UARS (mixing ratio)	ratio of precision from simulations to precision from scaling
UARS	O3	206.132	2.4E-05	3000	reference	reference	reference	reference	reference	1.6E-07	reference
UARS	ClO	204.352*	8.7E-03	2000	3.6E+02	0.7	2.9E-10	2.9E-10	3.9E-10	3.0E-10	0.8
EOS	Cl-35-O	649.451*	1.0E-01	12000	4.2E+03	4.0	1.5E-10				
EOS	Cl-35-O	204.352*	8.7E-03	4000	3.6E+02	1.3	5.4E-10	1.5E-10	1.9E-10	1.2E-10	0.6
EOS	H-35-Cl	625.919*	2.5E-01	12000	1.0E+04	4.0	6.1E-11	6.1E-11	8.2E-11	8.3E-11	1.0
EOS	CO	230.538	1.3E-04	4000	5.4E+00	1.3	3.9E-08	3.9E-08	3.9E-08	4.6E-08	1.2
EOS	HNO3	181.594*	5.60E-3	4000	2.3E+02	1.3	9.1E-10	9.1E-10	9.1E-10	9.0E-10	1.0
EOS	N2O	200.975	1.7E-04	4000	7.1E+00	1.3	3.0E-08				
EOS	N2O	652.834	1.1E-03	12000	4.6E+01	4.0	1.4E-08	1.3E-0.8	1.3E-08	1.5E-08	1.2
EOS	OH	2509.95*(H)	6.2E+00	30000	2.6E+05	10.0	6.2E-12				
EOS	OH	2509.95*(V)	6.2E+00	30000	2.6E+05	10.0	6.2E-12				
EOS	OH	2514.32*(H)	6.2E+00	30000	2.6E+05	10.0	6.2E-12				
EOS	OH	2514.32*(V)	6.2E+00	30000	2.6E+05	10.0	6.2E-12	3.1E-12	3.1E-12	4.4E-12	1.4
EOS	Br-81-O	624.768*	1.4E-01	12000	5.8E+03	4.0	1.1E-10				
EOS	Br-81-O	650.179*	1.4E-01	12000	5.8E+03	4.0	1.1E-10	7.8E-11	1.6E-10	1.1E-10	0.7
EOS	HO2	649.702	1.5E-02	12000	6.3E+02	4.0	1.0E-09				
EOS	HO2	660.486	2.4E-02	12000	1.0E+03	4.0	4.8E-10	4.3E-10	4.3E-10	1.9E-10	0.4
EOS	HOCl-35	635.870	2.7E-02	12000	1.1E+03	4.0	5.7E-10	5.7E-10	7.6E-10	3.8E-10	0.5
EOS	HCN	171.260	4.5E-02	4000	1.9E+03	1.3	1.1E-10	1.1E-10	1.1E-10	1.1E-10	1.0
EOS	SO2	204.247	1.5E-03	4000	6.3E+01	1.3	3.4E-09				
EOS	SO2	660.473	6.3E-03	12000	2.6E+02	4.0	2.4E-09				
EOS	SO2	660.918	6.5E-03	12000	2.7E+02	4.0	2.4E-09	1.5E-09	1.5E-09	7.6E-10	0.5

Acronyms

AFGL	Air Force Geophysics Laboratory
ATBD	Algorithm Theoretical Basis Document
DACS	Digital Auto-Correlator Spectrometer
DU	Dobson Unit
EOS	Earth Observing System
FOV	Field of View
IWC	Ice Water Content
MLS	Microwave Limb Sounder
UARS	Upper Atmosphere Research Satellite

References

AFGL, 'Handbook of Geophysics and the Space Environment', 1985.

A. Borysow and L. Frommhold, 'Collision-induced rototranslational absorption spectra of $N_2 - N_2$ pairs for temperatures from 50 to 300 K', Ap. J., 311, 1043–1057, 1986.

G. Brasseur and S. Solomon, 'Aeronomy of the Middle Atmosphere', 2nd ed., D. Reidel, Dordrecht, 1986.

EOS MLS Preliminary Design Review, Vol. 1, JPL D-15452, 1998.

K.L.S. Gunn and T.W.R. East, 'The microwave properties of precipitation particles', Quart. J. Roy. Meteorol. Soc., 80, 522–545, 1954.

A.E. Hedin, MSISE Model, 1990.

G. Hufford, 'A model for the complex permittivity of ice at frequencies below 1 THz', Int. J. Infrared Millimeter Waves, 12, 677–682, 1991.

R.F. Jarnot, 'EOS MLS Level 1 Data Processing Algorithm Theoretical Basis', JPL D-15210, Version 1.1, 15 October 1999.

J.S. Kinnersley and R.S. Harwood, 'An isentropic two-dimensional model with an interactive parametrization of dynamical and chemical planetary-wave fluxes', Quart. J. Roy. Meteorol. Soc., 119, 1167–1193, 1993.

H.J. Liebe, G.A. Hufford and M.G. Cotton, MPM93, 1993.

R. List, 'Smithsonian Meteorological Tables', 6th rev. ed., 1968.

N.J. Livesey and D.L. Wu, 'EOS MLS Retrieval Processes Algorithm Theoretical Basis', JPL D-16159, Version 1.1, 15 October 1999.

J.F. Muller and G. Brasseur, 'IMAGES – A 3-dimensional chemical-transport model of the global troposphere', J. Geophys. Res., 100(D8), 16445–16490, 1995.

A.H. Oort, 'Global Atmospheric Circulation Statistics', NOAA Professional Paper 14, Rockville, 1983.

H.M. Pickett, R.L. Poynter and E.A. Cohen, 'Submillimeter, Millimeter, and Microwave Spectral Line Catalogue', JPL Publication 80-23, Rev. 3, 1992.

H.C. Pumphrey, D. Rind, J. M. Russell III and J. E. Harries, 'A preliminary zonal mean climatology of water vapour in the stratosphere and mesosphere', Adv. Space Res., 21(10), 1417–1420, 1998.

W.G. Read, 'Microwave Limb Sounder (MLS) Direct Measurement Model for Radiative Spectral Intensity', Version 2.2, JPL, 1988.

W.G. Read, 'Microwave Limb Sounder (MLS) Spectroscopic Data Base', Version 2.0, JPL, 1992.

W.G. Read, 'EOS MLS Forward Model Algorithm Theoretical Basis', JPL D-nnnnn, Version DRAFT, 6 August 1999.

W.G. Read and Z. Shippony, 'Microwave Limb Sounder (MLS) Level Two Processing Coefficients Theoretical Basis', Version 2.0, JPL, 1991.

W.G. Read, L. Froidevaux and J.W. Waters, 'Microwave Limb Sounder measurement of stratospheric SO_2 from the Mt. Pinatubo volcano', Geophys. Res. Lett., 20(12), 1299–1302, 1993.

C.D. Rodgers, 'Retrieval of atmospheric temperature and composition from remote measurements of thermal radiation', Rev. Geophys. Space. Phys., 14, 609–624, 1976.

C.D. Rodgers, 'Characterization and error analysis of profiles retrieved from remote sounding measurements', J. Geophys. Res., 95(D5), 5587–5595, 1990.

L.S. Rothman *et al.*, 'The HITRAN molecular database – editions of 1991 and 1992', JQSRT, 48(5-6), 469–507, 1992.

B.J. Sandor, W.G. Read, J.W. Waters and K.H. Rosenlof, 'Seasonal behavior of tropical to mid-latitude upper tropospheric water vapor from UARS MLS', J. Geophys. Res., 103(D20), 25935–25947, 1998.

T. Shimazaki, 'Minor Constituents in the Middle Atmosphere', Terra Scientific, Tokyo, 1985.

S. Solomon *et al.*, 'Photochemistry and transport of carbon monoxide in the middle atmosphere', J. Atmos. Sci., 42(10), 1072–1083, 1985.

UARS Climatology, Version 3.1, 1994

J.W. Waters, 'Microwave Limb Sounding' in 'Atmospheric Remote Sensing by Microwave Radiometry', Ed. M.A. Janssen, Wiley, New York, 1993.

J.W. Waters, 'An Overview of the EOS MLS Experiment', JPL D-15745, Version 1.1, 15 October 1999.

J.W. Waters, W.J. Wilson and F.I. Shimabukuro, 'Microwave measurement of mesospheric carbon monoxide', Science, 191, 1174–1175, 1976.

J.W. Waters *et al.*, 'Validation of UARS Microwave Limb Sounder ClO measurements', J. Geophys. Res., 101(D6), 10091–10127, 1996.